Zircon double-dating, trace element and O isotope analysis to decipher late Pleistocene explosive-effusive eruptions from a zoned ocean-island magma system, Ascension Island

Jane H. Scarrow[1,2]*, Axel K. Schmitt[3,4], Martin Danišík[3], Katy J. Chamberlain[5], Bridie V. Davies[2], Jeremy Rushton[6], Richard J. Brown[7], and Jenni Barclay[2]

1. Department of Mineralogy and Petrology, University of Granada, 18071, Spain
(*corresponding author: jscarrow@ugr.es)
2. School of Environmental Sciences, University of East Anglia, Norwich, NR4 7TJ, UK
(J.Barclay@uea.ac.uk, Bridie.Davies@uea.ac.uk)
3. John de Laeter Centre, Curtin University, Perth, WA 6102, Australia
(axel.schmitt@curtin.edu.au, M.Danisik@curtin.edu.au)
4. Institute of Earth Sciences, Heidelberg University, Heidelberg 69120, Germany
5. Department of Earth, Ocean and Ecological Sciences, University of Liverpool, 4 Brownlow Street, Liverpool, L69 3GP, UK (K.J.Chamberlain@liverpool.ac.uk)
6. British Geological Survey, Nicker Hill, Keyworth, Nottingham NG12 5GG, UK
(jere1@bgs.ac.uk)

7. Department of Earth Sciences, University of Durham, DH1 3LE, UK

(richard.brown3@durham.ac.uk)

Highlights

- U–Th–Pb dating has identified recurrent felsic volcanism (1.34 Ma, 0.6 Ma, 95 ka).
- Eruption ages of the Echo Canyon explosive-effusive deposits converge at ca. 95 ka.
- Pre-eruptive zircon crystallisation occurred over ca. 10^3–10^4 from ca. 111–98.5 ka.
- Zircon trace element compositions indicate melt storage in discrete, zoned, lenses.
- Deposits of the most explosive phases sample lithic clasts from previous eruptions.

Abstract

In this first detailed study of zircon from Ascension Island, South Atlantic, we take a novel approach combining trace element and O isotope compositional data with double-dating (disequilibrium ^{238}U–^{230}Th and (U–Th)/He) to decipher timescales and dynamics of magmatic processes. The Echo Canyon (EC) sequence comprises small-volume explosive-effusive eruptions of trachyte that tapped a compositionally zoned magma system. Associated volcanic hazards may be constrained from the age of volcanism, duration of magma storage, and magma source and plumbing system character. Zircon U–Th–Pb dating of lithic lava clasts has revealed recurrent evolved volcanism at 1.34 and 0.6 Ma, and 95 ka. The (U–Th)/He zircon cooling ages indicate that most of the EC explosive-effusive sequence erupted in a brief episode at ca. 95 ka. Additionally, uniform ^{238}U–^{230}Th zircon crystallisation ages suggest moderately protracted magma storage with melt present at depth for at most 10^3–10^4 years before eruption. The enriched character of zircon trace element compositions, relative to MORB, in the absence of a continental crustal signature in the oxygen isotope values ($\delta^{18}O$ range 2.67–5.63‰), suggests the presence of an enriched component in the EC magma source. Furthermore, low $\delta^{18}O$ zircon compositions imply assimilation of high temperature hydrothermally altered country rock by the source magma. The mineral assemblage in crystal-poor pumices indicates equilibrium storage conditions: zircon saturation and Ti-in-zircon crystallisation temperatures are consistent with alkali feldspar-melt temperatures. Significantly, zircon crystals were preserved both as macrocryst inclusions and in the groundmass of EC explosive and effusive deposits. These rocks preserve evidence of magma evolution by fractional crystallisation. This process led to pre-eruptive compositional stratification, which is evidenced in the range of whole-rock major and trace element compositions and zircon Zr/Hf values. Notably, zircon crystallisation and cooling ages derived from pumice, lava, and accidental lithic lava clasts in highly explosive pyroclastic deposits, have revealed episodes of evolved magmatism that would otherwise have gone undetected. In addition, the zircon trace element and isotope compositions, in combination with the range of crystallisation ages, evidence progressively deeper tapping of less evolved magma stored in discrete lenses. Thus, a combined zircon geochronological-geochemical approach can place constraints on the recurrence ca. 0.6 Ma, millennial to decamillennial duration, enriched source and explosive-effusive style of past eruptive pulses. This information is relevant for assessing hazards and informing monitoring and forecasting efforts to assist in managing associated risks for small ocean island volcanoes with particularly vulnerable populations and infrastructure.

Keywords: Quaternary, South Atlantic, tephrochronology, chronostratigraphy, radiogenic isotopes, U-series, (U–Th)/He, ocean island volcanism, trachyte, pumice.

65 **Graphical abstract**

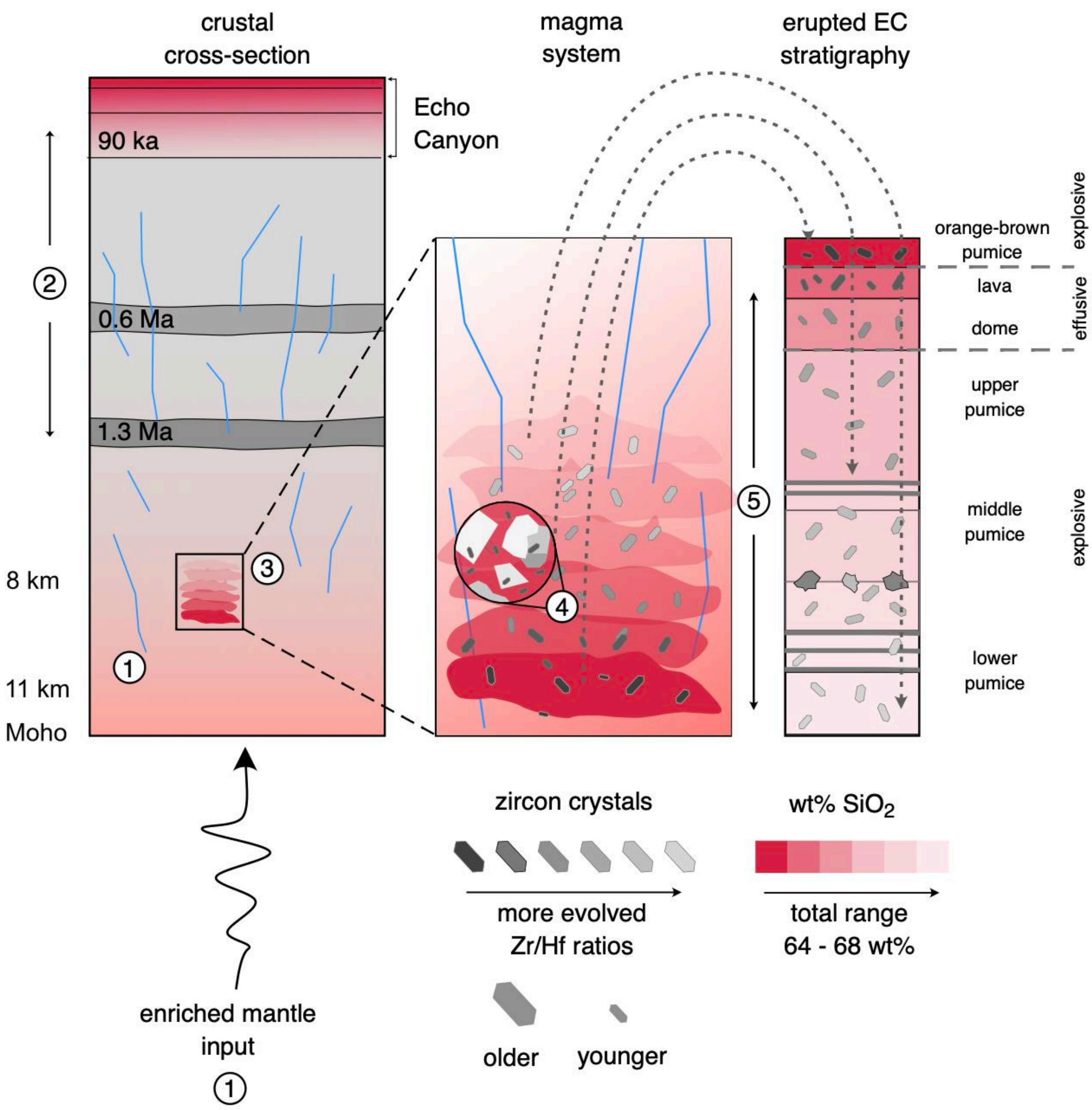

66

1. Introduction

Dating Quaternary magmatism is a geochronological challenge. The application of available methods, including radiocarbon ^{14}C, $^{40}Ar/^{39}Ar$, fission-track and luminescence dating, can be complicated by the lack of (i) available datable materials (e.g., preserved organic material or K-rich minerals, Hughen, 2007), (ii) open-system processes (e.g., post-magmatic hydration or Ar loss, Albarede et al., 1978), and (iii) difficulties in precisely measuring low intensity signals (e.g., low Th and Pb concentrations in zircon, Schaltegger et al., 2015; also see Dosseto et al., 2011, and references therein, for an overview of dating methods applications and limitations). Nonetheless, forecasting when and how a volcano may erupt is informed by its past behaviour, and thus reliable ages for previous eruptions are critical to long-term planning and hazard mitigation. In this context, we focus on the chronostratigraphy and pre-eruptive magmatic character of the only documented explosive-effusive transition on Ascension Island, South Atlantic. This British Overseas Territory (Fig. 1) is a key strategic staging point for ships and aircraft and hosts a population of ~1000 along with British and US military bases and key communications assets. In-depth study of volcanism on the island is particularly timely because the magmatic system has recently been classified as active based on an $^{40}Ar/^{39}Ar$ basalt groundmass age of 0.51±0.18 ka (Preece et al., 2018, 2σ analytical uncertainty, here and throughout unless otherwise stated).

When deciphering magmatic processes, the accessory mineral zircon, commonly present in intermediate-felsic igneous rocks, is particularly useful because (i) it records both geochronological and compositional information, and (ii) it is chemically and physically resistant to subsequent magmatic and post-eruptive processes (Hanchar and Hoskins, 2003). Consequently, one potential pathway to characterise Quaternary volcanic activity is to combine zircon compositional analysis and geochronology. Magma source character and system processes are constrained by O isotope and trace elements; whereas, timing of zircon crystallisation and eruption is determined by zircon double-dating (ZDD), i.e., U–Th–Pb or disequilibrium ^{238}U–^{230}Th crystallisation ages linked to (U–Th)/He cooling ages (Schmitt et al. 2006; Danišík et al., 2017). This methodology has the ability to date zircon grains to ca. 2 ka (Marsden et al. 2021). Therefore, it can be applied to a gap in Quaternary geochronology to determine the age of samples that are: older than the upper limit of ^{14}C dating, >50 ka, and younger than the lower limit, ca. 1 Ma, of traditional dating methods (Dosseto et al., 2011). Furthermore, the U–Th–Pb and (U–Th)/He systems have different closure temperatures, >900°C and ~180°C, respectively (Cherniak and Watson, 2001; Reiners et al., 2004). These differences permit estimation of zircon residence times in magma systems constraining their longevity and cyclicity. Hence, volcanic hazard assessment, monitoring and forecasting and so risk mitigation can be informed by ZDD studies (e.g., Danišík et al., 2020; Friedrichs et al., 2020; Marsden et al., 2021; Cisneros de León et al., 2023).

In recent years, several studies have investigated zircon as a geochronometer and indicator mineral for igneous processes in oceanic island settings such Ascension (e.g., Carley et al., 2011; Sagan et al., 2020; Rojas-Agramonte et al., 2022). However, to date ZDD has only been used for one ocean island, Piton des Neiges, Réunion Island (Famin et al. 2022), as part of a multi-pronged geochronological approach combining zircon U–Pb, phlogopite ^{40}Ar/^{39}Ar, and zircon and apatite (U–Th)/He dating. Zircon crystallisation is principally promoted by decreasing magmatic temperature and melts reaching evolved compositions (e.g., Watson and Harrison, 1983; Shao et al., 2019). However, because basalts (OIBs) are often predominant in ocean island settings, rocks from these regions are commonly zircon undersaturated. Nonetheless, zircon is increasingly detected in ocean island settings, where it falls into three main categories, each of which has potential to be applied to evaluation of geochronological changes in the system if interpreted within an appropriate compositional and textural context: (i) part of the stable mineral paragenesis as microcrystic zircon in volumetrically minor evolved alkaline magmas and grains crystallising from late-stage segregations of felsic melt (Carley et al., 2011; Padilla et al, 2016; Rojas-Agramonte et al., 2022; Scarrow et al., 2022); (ii) antecrysts recycled from precursor plutonic or volcanic rocks which are often significantly older than the host rocks but clearly related to OIB magmatism (Vazquez et al., 2007; Bindeman et al., 2012; Banik et al., 2021; Rojas-Agramonte et al., 2022); and (iii) exotic zircon, xenocrysts, inherited from extraneous and ancient sources for which mantle asthenosphere (Rojas-Agramonte et al., 2022) or continental lithosphere (Torsvik et al., 2013; Sagan et al., 2020; Greenough et al., 2021; Rolim, 2022) have been suggested. Clearly, remobilisation and reinitiation of zircon crystallisation in (ii) and (iii) may result in a progression of ages within a single grain with potential to reach (i) stable mineral paragenesis. In the third case care must be taken to determine that such crystals are not derived from sampling- or laboratory-based contamination but instead truly inherited and heated by their host magmas. The latter can be identified, for example, from evidence of radiation damage detected by Raman spectroscopy (e.g., Bjerga et al., 2022) or age resetting identified by (U–Th)/He dating (e.g., Famin et al., 2022). The majority of zircon crystals from Ascension Island considered here fall in the first category with a few grains from the second.

In this first detailed study of Ascension Island zircon, originally identified by Daly (1925), we combine data from fieldwork, petrographic study and mineral and whole-rock analysis with ZDD and zircon O isotope and trace element compositional analyses to constrain the temporal association of the Echo Canyon (EC) explosive-effusive stratigraphic sequence and characterise its pre-eruptive magma evolution. By shedding light on the longevity of magma storage, source character and magma plumbing processes, our data place constraints on the chronostratigraphy and petrogenesis of this Pleistocene explosive-effusive volcanic sequence. The EC deposits contain exclusively Pleistocene-aged zircon which crystallised shortly before eruption; whereas zircon in the accidental lithic clasts from the deposits record earlier felsic magmatic phases that had previously gone undetected.

2. Geological setting and field relations

Ascension Island is a small composite ocean island volcano located in the south Atlantic (7° 56 'S; 14° 22 'W) (Fig. 1). It lies ~100 km west of the Mid-Atlantic Ridge and 50 km south of the Ascension Fracture Zone. Built on 5–7 Ma ocean crust it has subaerial dimensions of 8 km by 12 km; the last 1 Myr of subaerial volcanism represents a fraction of the 5–6 Ma volcanic edifice (Klingelhofer et al., 2001). It is unclear whether the magmatism is related to, although not centred on, a diverted shallow low flux mantle plume (Gaherty and Dunn, 2007) or to anomalously enriched, relative to MORB, Mid-Atlantic Ridge type mantle displaced by westward plate movement (Paulick et al., 2010). Compositionally diverse picrites–comendites have erupted as effusive and explosive volcanic deposits (Weaver et al., 1996; Chamberlain et al., 2019; Davies et al., 2021) with mafic–felsic volcanic and plutonic clasts (Harris, 1983; Kar et al., 1998). Our focus is on what is currently considered to be the youngest known felsic volcanic deposit on the island, recently dated at 59±4 ka by feldspar $^{40}Ar/^{39}Ar$ (Preece et al., 2021): the EC explosive-effusive sequence.

Davies et al. (2021) presented a detailed textural study of EC juvenile pumice clasts and lavas to characterise the transition from explosive to effusive eruptive activity. From the base to the top, the sequence comprises a proximal pumice cone with rare decimetre-scale trachyte and rhyolite lava clasts embedded between the clasts in the pumice deposits, an endogenous effusive post-cone lava dome, brecciated lava, and a capping orange-brown pumice deposit (Fig. 2). A lack of field evidence for temporal breaks in the sequence and distinctive large alkali feldspar macrocrysts in all the rocks led Davies et al. (2021) to interpret the deposits as products of a single eruption with an estimated dense rock equivalent volume of 0.01–0.3 km^3. The lower cone comprises ~10 m of angular to sub-angular, clast-supported, pumice fall with a modal clast size that increase up sequence from 2–3 cm to 4 cm diameter (maximum 30 cm) and rare angular fragmented bombs up to 50 cm diameter. Conformably overlying these deposits, the middle cone is composed of ~2 m of angular sub-angular clast-supported pumice fall that becomes ashier, matrix-supported, upwards then transitions into an uppermost clast-supported layer. The middle cone clasts are smaller, having a modal diameter of 0.5–2 cm (maximum ~30 cm) near its base, reducing to 0.5–1 cm higher up; again, angular-fragmented bombs, which are uncommon, are up to 30 cm in diameter. The lower section of the upper cone deposits is ~30 m thick varying from ash-rich containing only ~20% pumice clasts to clast-rich with ~60% ~sub-rounded to rounded juvenile lapilli; the modal clast size is 5 cm and bombs have up to 40 cm diameters. The uppermost upper cone is ~15 m thick comprising angular pumice clasts which decrease in diameter from 12–4 cm up sequence and bombs that are elongated up to 70 cm. Directly above the cone, the post-cone deposits include the 30–40 m thick, fine-grained, brecciated porphyritic trachyte dome and ~10 m thick brecciated lava. At the top of the EC sequence the 3–10 m thick clast-supported orange-brown-pumice is formed of larger, ~10 cm diameter, angular clasts and sparse bombs (maximum diameter ~45 cm). See Davies et al. (2021) for detailed descriptions of all units.

3. Samples, materials and methods

Supplementary material includes full details of methods, precision, and accuracy as well as complete data sets for whole-rocks (major and trace elements) and zircon (U–Th–Pb, ^{238}U–^{230}Th disequilibrium, (U–Th)/He, O isotopes, and trace elements.

Detailed study was undertaken of seven samples of the EC explosive-effusive transition pumice and lava units, each composed of composites of clasts collected from uniform horizontal layers, as well as three accidental lithic lava clasts excavated from within the juvenile pumice (Fig. 2). From base to top of the stratigraphic sequence, following the nomenclature of Davies et al. (2021) these samples are: lower cone - pumices (samples 842, 843, 844), middle cone - pumice (sample 829); and post-cone - dome (sample 871), lava breccia (sample 828) and orange-brown pumice (sample 827) (Fig. 2). Pre-cone accidental lava clasts (samples 844F1, 844F2 and 844F3) were sampled from a lithic-rich band between lower pumices 843 and 844.

Thin sections were made of samples for petrographic examination. Remaining material was prepared for geochemical analyses and mineral extraction. Splits from all ten samples were powdered for whole-rock major element X-ray fluorescence analysis in a tungsten-carbide ring mill at the University of East Anglia, U.K.; for elements with concentrations >0.5 wt.% analyses of multiple international standards yielded uncertainties ≤ ±0.5 wt.% (2σ), except for SiO_2 which yielded uncertainties of ±1.06 wt.% (2σ). Major element data are plotted normalised to 100 wt % dry totals. Rare earth elements plus selected trace elements were analysed by ICP-MS at the University of Granada, Spain, Scientific Facilities Centre (UGR-CIC); precision, as determined from international standards, was better than ±2% and ±5% for concentrations of 50 and 5 ppm, respectively.

Zircon was extracted from seven samples by crushing, sieving using synthetic mesh, then panning the 50-250 μm fraction in water to concentrate heavy minerals. This concentrate was refined by magnetic separation and dissolution of other silicates and phosphates with a mixture of hydrochloric and hydrofluoric acid before hand picking using a binocular microscope. Grains were mounted in epoxy, polished, coated with carbon and then imaged using a scanning electron microscope (SEM). The SEM contrast and brightness settings were constant for all cathodoluminescence analyses permitting comparison of relative intensities between samples. Semi-quantitative SEM compositional scans to locate accessory phases were undertaken of thin sections at the British Geological Survey, U.K. Zircon was analysed for ^{238}U–^{230}Th for two of the three lithic clasts analysed for major and trace elements as well as for three pumice, one dome and one lava samples at the Heidelberg Ion Probe laboratory, Heidelberg University, Germany. The two lithic clast samples with zircon in secular equilibrium were also dated by U–Th–Pb methods at the same facility. Data accuracy is ascertained by analysis of zircon references: for AS3 (Paces and Miller, 1993), secular equilibrium (^{230}Th)/^{238}U) values within error of ±2% of unity were determined in two analytical sessions (n = 33), whereas for 61308 a ^{206}Pb/^{238}U age of 2.65 ± 0.07 Ma (n = 10) was obtained in comparison to the reported age of 2.5 Ma (Wiedenbeck et al., 1995). Four samples of the samples dated by U–Th–Pb methods (lower pumice, orange-brown pumice, dome and lava) were also analysed for (U–Th)/He at the John de Laeter Centre, Curtin University, Australia (Table 1); and two samples for O isotopes (lower pumice, n = 20, and dome, n = 20) at the UGR-CIC Sensitive High Resolution Ion Microprobe (SHRIMP) IBERSIMS laboratory with correlative trace elements determined by LA-ICPMS at the UGR-CIC. Unless otherwise stated, all age uncertainties are quoted at 2σ in the text; 1σ errors are plotted for clarity.

4. Results

4.1 Whole-rock petrography and composition

Detailed descriptions of the petrography of the EC pumice, dome and lava can be found in Davies et al. (2021); whole-rock data for the seven volcanic deposits and three lithic clasts are presented in Fig. 3. All pumices are hypohyaline whereas the lava and dome are hypocrystalline. Microlites, <10–200 μm, which are predominantly albite, comprise ~1-2 modal % in pumice, although there are patches of up to ~70 modal % in the dome, ~30 modal % in the lavas and >60 modal % in the orange-brown pumice (Davies et al., 2021). The glass-rich pumices have rare, but distinctive, <1 modal %, 2–4 mm, crystals of albite to anorthoclase feldspar and clinopyroxene that, in places, form 3-8 mm glomerocrysts; lavas have up to 5 modal % of these same minerals. Vesicularity varies from 65–95% at the base of the sequence to 50–95% in the upper pumices (Davies et al., 2021). The cone pumices contain zircon and other accessory phases including baddeleyite, barite, monazite, chevkinite and Fe sulphides; apatite was not detected. The post-cone dome and lava breccia contain zircon and apatite as well as the other accessory phases observed in the cone pumices. The post-cone orange-brown pumice from the top of the sequence has the same accessory phases as the lower cone pumices.

All the samples, except one rhyolitic lithic clast (RLC), are trachytic with an alkaline metaluminous character (SiO_2 64.3–68.3 wt % and Na_2O+K_2O 10.8–12.4 wt %; RLC SiO_2 74.3 wt % and Na_2O+K_2O 9.8 wt %) (Fig. 3A). Normalised to chondrite, all samples are enriched in light rare earth elements (LREE) relative to heavy rare earth elements (HREE). The lower cone pumices have higher concentrations of all REE than the upper cone deposits and a marked negative anomaly in Eu which is absent in the samples from the top of the sequence (Fig. 3B); the RLC has a lower concentration parallel REE pattern. Notably, the samples from the base of the pumice cone sequence, below the lava breccia, have the highest SiO_2, K_2O, Zr, Hf, and Rb, as well as lowest TiO_2, Al_2O_3, MgO, FeO, CaO, Na_2O, Sr, Ba and Eu. Major elements, except K_2O, correlate negatively with SiO_2, whereas all trace elements, except Sr, Ba and Eu, correlate positively (Fig. 3C-D). Both the orange-brown pumice and lithic clasts lie off the major and trace element trends defined by the lower pumice to dome sequence (Fig. 3).

4.2 Zircon texture, composition and geochronology

4.2.1 Texture

Zircon grains in the volcanic lithic clasts are euhedral-subhedral, 50–100 μm in length, transparent, colourless, unzoned and with intermediate cathodoluminescence intensities (see supplementary material file Scarrow et al_supp mat_zircon CL images). Zircon grains in all explosive-effusive juvenile samples are euhedral-subhedral, equidimensional to tabular with rare pyramidal terminations and are 50–150 μm in length and with comparable optical properties to those in the lithic clasts. They have weak to intermediate cathodoluminescence intensities, with both oscillatory and sector zoning (see aforementioned supplementary material file). No textural evidence was detected in any of the zircon grains for more than one stage of growth, e.g., inherited cores, resorption surfaces or overgrowth rims. One larger grain, ~250 μm in length, was found in the cone lower pumice and several grains up to 200 μm in length were identified in the dome samples. In addition to the 50–100 μm, subhedral grains present in all juvenile explosive-effusive samples, the post-cone dome, lava breccia and orange-brown pumice samples also have a second population of zircon grains of acicular euhedral morphology and pyramidal terminations, but only ~20–30 μm in length. High-resolution SEM imaging has revealed that in all samples, in addition to being present entrained as inclusions in macrocrysts, zircon is present in the glassy matrix of pumice and the microcrystalline lava groundmass.

4.2.2 Composition

O isotopes

Oxygen isotopes were measured in grains from two selected samples: the cone lower pumice and the post-cone dome (Fig. 4A). Values for $\delta^{18}O$ (reported relative to VSMOW) are heterogeneous and range from well below to within the range of typical of mantle zircon (5.3±0.6‰) (e.g., Valley, 2003). The lower pumice range is broader (2.67–5.20‰, n = 20) whereas the dome $\delta^{18}O$ range is more restricted (3.40–5.63‰, n = 20), but still larger than the analytical uncertainties of 0.14‰. The variations in $\delta^{18}O$ are uncorrelated with differentiation indices such as (Zr/Hf), Eu anomalies, or age.

Trace elements

Zircon from the same two samples analysed for O isotopes show significant composition differences for trace elements (Fig. 4B). The REE concentrations in each of the two analysed samples vary by an order of magnitude, comparable with typical intra-grain and inter-grain compositional variations in other magmatic zircons (cf., Hoskin and Schaltegger, 2003) (Fig. 4C, supplementary material 'Zircon trace elements'). The spread of REE is more restricted in the lower pumice than in the dome (Fig. 4C). However, all the zircon chondrite-normalised REE patterns are parallel-subparallel and have similar, typically igneous zircon concentrations: depletion in LREE relative to HREE ($[Gd/Yb]_N$ 0.05–0.15) (cf., Hoskin and Schaltegger, 2003); and positive Ce and negative Eu anomalies relative to adjacent REE, indicating, paradoxically, that Eu^{2+} and Ce^{4+} can coexist in zircon-saturated magmas (Trail et al., 2012). The zircon Eu anomalies in both samples are moderately negative with Eu/Eu* between 0.08 and 0.39 (Eu = Eu_N and Eu* = $[Sm \times Gd]^{0.5}$). Trail et al. (2012) noted Eu anomalies of zircon crystallised from the same melt composition are more negative at lower oxygen fugacities but, also, that such anomalies may reflect melt compositions. Significantly, therefore, although Eu depletion has typically been attributed to plagioclase fractionation under reducing conditions prior to zircon crystallisation (Hoskins and Ireland, 2003; Cisneros de León et al., 2019), this is not required to produce a negative Eu anomaly in zircon (Trail et al., 2012). The Eu/Eu* values of the EC dome zircon are more heterogeneous than those of the lower pumice, although in the whole-rock data, a negative Eu anomaly is only evident in the most evolved lower pumice sample. The EC zircon Ce anomalies, on the other hand, are similarly strongly positive in both samples, Ce/Ce* = 11.5–195.3 (where Ce = Ce_N and Ce* = $[La \times Pr]^{0.5}$) (Fig. 4C). Such anomalies increase with higher oxygen fugacities and lower crystallisation temperatures in the magmatic system (Trail et al., 2012) and are also dependent, to a lesser extent, on the melt water content and composition (Smythe and Brenan 2015). The whole-rock data, on the other hand, show absent or very weakly positive Ce anomalies (Fig. 4C). Some of the small, ~20 μm crystals in the dome are exceptionally high in REEs (Ce 2–8 wt %) with elevated La values atypical of magmatic zircon (Hoskin and Schaltegger 2003; Claiborne et al. 2010; Ni et al. 2020). This may reflect tiny inclusions of LREE-rich minerals, e.g., allanite or chevkinite.

Other zircon trace element concentrations are also heterogeneous: ranging from evolved compositions (U/Yb >0.7, Hf ~18,000 ppm, and Yb ~3000 ppm) in the lower pumice to almost typical MORB zircon values in the dome with U/Yb <0.1 (Grimes et al., 2015), Hf ≤ 9000 ppm and Yb ≤ 700 ppm. Uranium abundances are generally higher in the lower pumice than in the dome, albeit with considerable overlap, 482–1023 ppm and 182–809 ppm respectively; the Th/U ratio average, 0.9±0.3, is typical of igneous values ≥0.5 (Hoskin and Schaltegger, 2003). The MREE-HREE and Y show the same relative variation as U in the two samples, being higher in the lower pumice than in the dome which reflects the differences in the whole-rock compositions. Titanium values in the lower pumice range from 6.4–26.3 ppm but are excessively high in the dome zircon. This suggests beam overlap onto microscopic inclusions of Ti-rich minerals such as Fe-Ti oxides or titanite.

Zircon crystallisation and fractionation depletes Zr in the melt relative to the slightly less compatible Hf, so as a zircon-saturated magma evolves, Hf concentrations increase in the melt and in the crystallising zircon so that decreasing Zr/Hf is an index of differentiation (Claiborne et al., 2006). The EC zircon range of Zr/Hf values is consistently less in the lower pumice than the dome, with ratios of 27.4–38.6 and 45.5–90.4, respectively. Nevertheless, Zr/Hf only varies systematically with a few elements: Sc shows a clear negative correlation (Fig 4B) as do Y and the MREE-HREE. However, the relative concentrations of MREE and HREE, recorded by $(Gd/Yb)_N$, remain constant as Zr/Hf changes with evolving melt composition. All EC whole-rock Zr/Hf values are higher than chondrite between 42.7 and 56.2 (supplementary material, 'Whole-rock majors and traces').

In the Grimes et al. (2015) tectonomagmatic discrimination diagram (Fig. 4D), the more evolved, higher Hf, lower pumice zircon grains plot along a melt fractionation trend from the dome compositions which fall predominantly in the high U/Yb Iceland-Hawaii hotspot 'crustal input or enriched mantle source' field.

4.2.3 Geochronology

^{238}U–^{230}Th disequilibrium and U–Th–Pb data and crystallisation ages – volcanic clasts

High-resolution secondary ion mass spectrometry (SIMS) ^{238}U–^{230}Th results indicated secular equilibrium for zircon from two samples of rare decimetre-scale angular volcanic lithic clasts sampled within the lower pumice with $(^{230}Th)/(^{238}U) = 1.004 \pm 0.070$ (MSWD = 0.67; n = 14; Fig. 5E). After ^{207}Pb-based common Pb-correction and accounting for initial deficit in ^{230}Th the U–Th–Pb zircon dates yielded single grain dates that range from 0.47–0.65 Ma (sample 844F2), and 1.01–2.34 Ma (sample 844F3), with weighted averages of 0.610 ±0.08 Ma (MSWD = 0.83, n = 3) and 1.34 ±0.13 Ma (MSWD = 0.80, n = 11), respectively (Fig. 6).

^{238}U–^{230}Th disequilibrium data and crystallisation ages – explosive-effusive sequence

Zircon SIMS ^{238}U–^{230}Th disequilibrium dates (Table 1, Fig. 5) were calculated from free-fit isochrons in (^{230}Th)/(^{232}Th) – (^{230}Th)/(^{238}U) space for each sample. Two-point model isochron dates were computed using corresponding whole-rock U and Th abundances assuming secular equilibrium for comparison, but the zircon isochrons are the most robust ages because they are independent of assumptions on the melt composition from which zircon crystallised. The ^{238}U–^{230}Th disequilibrium dates, interpreted as crystallisation ages, from the base to the top of the sequence are: cone lower pumice (sample 842) 108 +10/-9 ka (MSWD = 0.79, n = 17), lower pumice (sample 844) 113 +15/-14 ka (MSWD = 0.77, n = 16), and post-cone dome (sample 871) 111 +4/-4 ka (MSWD = 0.68, n = 55). The overlying lava breccia (sample 828) yields an isochron age of 108 +2/-2 ka (MSWD = 0.94, n = 34), whereas the orange-brown pumice (sample 827) produced an isochron date of 98.5 +5.9/-5.6 ka (MSWD = 0.85, n = 39) for the dominant zircon population. Notably there is no significant difference between the large and the small zircon population dates. The only grains excluded from the isochron calculations were in the orange-brown pumice 827 (two young model dates of ca. 60 ka as well as two older dates at ca. 180 ka, Fig. 5A) and in lower pumice 844 (one older zircon plotting on the equiline; Fig. 5D). Uniformity of the zircon crystallisation ages is indicated by the near unity MSWD when averaging dates from all juvenile samples, only excluding the aforementioned grains from samples 827 and 844. The resulting isochron age of 106 +2/-2 ka (MSWD = 1.24, n = 162) suggests a brief interval of zircon crystallisation in the EC magma system.

(U–Th)/He data and eruption ages – explosive-effusive sequence

Zircon crystals from four representative samples of the explosive-effusive transition (Table 1) were dated by the (U–Th)/He method. The (U–Th)/He dates, corrected for alpha-ejection and for disequilibrium deficits in ^{4}He, are younger than their corresponding ^{238}U–^{230}Th ages for all 63 double-dated crystals (Fig. 7). The (U–Th)/He weighted mean ages (arranged in stratigraphical order from bottom to top) are: cone lower pumice (sample 842) 81.7±8.8 ka (MSWD = 1.4; n = 8); post-cone dome (sample 871) 91.7±6.2 ka (MSWD = 0.37; n = 10); post-cone lava breccia (sample 828) 96.3±9.3 (MSWD = 6.1; n = 17; one crystal at ca. 57 ka excluded as a statistical outlier, see section '5.1.3 (U–Th)/He zircon eruption ages' below for discussion); and post-cone orange-brown pumice (sample 827) 96.9±3.8 ka (MSWD = 1.1; n = 24; three crystal averaging at ca. 43 ka excluded as statistical outliers, see section '5.1.3' below for discussion). These (U–Th)/He weighted mean ages overlap within analytical uncertainties for the three samples from the base of the stratigraphic section and for the three samples from the top of the stratigraphic section, suggesting a single eruptive sequence lacking significant time breaks.

To reconstruct a robust eruptive chronology for the dated deposits and to better estimate the eruption ages and quantify uncertainties, we employed ChronoModel v. 2.0 software (Lanos and Dufresne, 2019) to develop a Bayesian age sequence model that incorporates not only ZDD geochronological data but also stratigraphic information (Danišík et al., 2020). Bayesian age sequence modelling results integrate the measured (U–Th)/He weighted mean ages and associated uncertainties and stratigraphic information. This modelling suggests the following eruption ages and uncertainties for the dated samples (stated as maximum *a posteriori* probability, MAP, ± 95% highest posterior density, HPD): lower pumice (sample 842) 99.7 +1.3/-8.2 ka; dome (sample 871) 96.6 +8.4/-9.2 ka; lava breccia (sample 828) 95.1 +6.8/-11.2 ka, and orange-brown pumice (sample 827) 93.9 +5.9/-19.3 ka (Fig. 8). For interpretation purposes, we will adopt these values as our best estimates for eruption ages. These eruption ages are in most cases within error of the ^{238}U–^{230}Th dates, which correspond to pre-eruptive crystallisation in the melt. The only exception is the lava breccia where the eruption age of 95.1 +6.8/-11.2 ka resolvably postdates the average zircon crystallisation age of 108 +4/-4 ka for this sample, which has the lowest age uncertainty of the investigated samples.

4.2.4 Intensive variables

Zircon crystallisation temperatures and oxygen fugacity

Ti-in-zircon thermometry (Watson and Harrison, 1983; Ferry and Watson, 2007) could only be undertaken for the lower pumice not the dome. The latter has excessively high Ti values, attributed to microscopic inclusions of Ti-rich minerals such as Fe-Ti oxides and titanite. A silica activity a(SiO2) of 0.75 was assumed for the calculations because angular quartz microcrysts have been detected in the groundmass of both the dome and lava (Davies, 2021) but not in the lower pumice. Furthermore, coexisting oxides have not been analysed in the EC rocks so Ti activity, $a(TiO_2)$ cannot be calculated by this method. However, rutile is not present in the rocks and titanomagnetite is markedly more abundant than ilmenite in other Ascension Island rocks (e.g., Chamberlain 2016, 2019). Thus, a relatively low $a(TiO_2)$ may be assumed since, if Ti were freely available in this Fe-rich system, ilmenite would crystallise in preference to magnetite. Using the equations of Ghiorso and Evans (2008) for Fe-Ti oxides from a, geographically close and compositionally similar, zoned pumice fall, Chamberlain et al. (2016) calculated: a(TiO2) = 0.37 (range 0.32-0.4). Using this value yields an average Ti-in-zircon temperature of 930°C with a range of 850–1020°C (temperature calculated according to Ferry and Watson 2007, with pressure dependence according to Ferriss et al., 2008). Higher Si activity would increase the Ti-in-zircon temperature ($aSiO_2$ = 1.0, ~40°C higher) whereas higher Ti activity would decrease the calculated temperature ($aTiO_2$ = 0.5, ~40°C lower).

Oxygen fugacity of the lower pumice magma as zircon crystallised was calculated to be in the range ΔFMQ +1.38 to +3.77 using the Loucks et al. (2020) calibration based on zircon Ti, U and Ce concentrations.

Zircon saturation temperatures

Zircon crystallisation is controlled by temperature and magma composition, specifically, the Zr content and the M value (cation ratio (Na + K + 2Ca)/(Al × Si)). The EC whole-rock zircon saturation temperatures (ZST), calculated using the equations of Boehnke et al. (2013), are high: cone pumices (920°C), which is comparable to the lower pumice average Ti-in-zircon temperature of 930°C (Ferry and Watson 2007). A clear distinction is evident, though, between the cone pumice ZST and the lower ZST values (845°C-865°C) of all the post-cone samples – effusive lava breccia, orange-brown pumice and dome – as well as the older trachytic accidental volcanic lithic clasts.

5. Discussion

The zircon double-dating, trace element and O isotope results are combined with whole-rock data to investigate the chronostratigraphy of the Echo Canyon explosive-effusive volcanic deposits. In particular, the temporal association of the sequence requires discussion, as well as the magma source and pre-eruptive processes that may be inferred from the zircon data.

5.1 Insights into magmatic processes from zircon geochronology: magma storage – crystallisation and eruption timing

5.1.1 U–Th–Pb zircon crystallisation ages

The U–Th–Pb crystallisation ages for zircon from the volcanic lithic clasts evidence earlier phases of evolved effusive volcanic activity at EC: 1.34±0.13 Ma and 0.610±0.08 Ma (Fig. 6). Based on the compositional similarity with the explosive-effusive deposits of the current study (Fig. 3), these volcanic lithic clasts are interpreted to be derived from previous eruptive events and because of their large size, their source must be proximal. The older age is coeval with the most ancient Ascension Island subaerial volcanism (Weaver et al., 1996; Jicha et al., 2013). However, it is the first identified record of such old activity in the east of the island. A recent study by Preece et al. (2021) concluded the Ascension Island felsic subaerial eruptions had marked geographical differences: ca. 1000—500 ka in the Central Felsic Complex and ca. 100—50 ka in the Eastern Felsic Complex where EC is located (Fig. 1). Therefore, the EC lava clast ages, 60—1300 ka, indicate felsic volcanism was more widespread in the early sub-aerial history of the east of the island than previously recognised as a result of lack of surface exposure, warranting further investigation into volcanic lithic clasts. As noted by Preece et al. (2021) the >80 identified felsic explosive eruptions are likely a minimum estimate because of poor preservation related to erosion, covering of deposits by later volcanic activity, and deposition of tephra in a marine rather than terrestrial context. Eruption cyclicity may be elucidated by dating of zircon-bearing volcanic lithic clasts commonly found in explosive deposits across the island (authors' unpublished data). Moreover, the age and distribution of subsurface magmatism, recorded in plutonic lithic clasts, is of particular relevance because crustal heterogeneity apparently exerted a significant control on the fractional crystallisation of small-volume magma batches on Ascension Island (Chamberlain et al., 2019), thus, affecting the evolution of this and, by inference, other similar ocean island systems. Notably, zircon grains in secular equilibrium, i.e., >350 ka, were only detected in one of more than 160 crystals analysed for ^{238}U–^{230}Th in the five samples of EC explosive-effusive juvenile pumice and lava.

5.1.2 ^{238}U–^{230}Th disequilibrium zircon crystallisation ages

The EC explosive-effusive transition sequence displays zircon isochron dates of 108–113 ka that represent a brief crystallisation interval, which also constrains the maximum eruption age for these deposits (Fig. 5). Comparing crystallisation and eruption ages indicates preservation of zircon formed over 10^3–10^4 a, and crystal residence ages of 19±10 kyr for sample dome 871 for which most data are available. Overlap, within error, of zircon ages from the EC juvenile pumice, lava breccia and dome indicates that the explosive effusive transition sequence tapped the same magmatic system. In addition, the lava breccia contains coeval smaller, 20–30 μm, zircon crystals which likely crystallised shortly before the eruption. These crystallisation ages are contemporaneous with feldspar $^{40}Ar/^{39}Ar$ ages for a 110±13 ka zoned pumice-scoria fall deposit (Chamberlain et al., 2016; Preece et al., 2021), that crops out on the coast ~1 km northeast of EC and a 105 ± 9 ka pumice fall, ~3 km to the southeast (Preece et al., 2021).

The EC sequence-capping orange-brown pumice, however, yielded a marginally younger zircon ^{238}U–^{230}Th isochron age of 98.5 ka (Fig. 5A), which is consistent with the interpretation of this deposit as a late-stage post-cone, post-effusive, short-lived explosive phase (Davies et al., 2021). This unit is also distinctive in that it contains rare zircon crystals with older (ca. 180 ka) and younger (ca. 60 ka) ^{238}U–^{230}Th model ages. Synchroneity between the two younger zircon ^{238}U–^{230}Th model crystallisation ages in the capping orange-brown pumice and the published EC feldspar ^{40}Ar/^{39}Ar age, ca. 60 ka, which dates the lower pumice unit (K.J. Preece, pers. comm.), indicates the presence of evolved melt in the Ascension Island magma system at that time. This age also overlaps with explosive eruptions such as Devil’s Cauldron with 62 ± 8 ka and 65 ± 7 ka feldspar ^{40}Ar/^{39}Ar ages (Preece et al., 2021) that overlies the EC sequence 1.5 km to the south.

5.1.3 (U–Th)/He zircon eruption ages

The (U–Th)/He dates mark the time since the zircon crystals passed below ~180°C, i.e., a cooling age, generally considered to be related to eruptive quenching or intermittent heating at the time of eruption causing older crystals to reset (Reiners et al., 2004). Measured (U-Th)/He dates were corrected for initial disequilibrium and potential crystal residence using the ZDD approach (Danišík et al., 2017), and together with available stratigraphic information used for Bayesian age sequence modelling to estimate eruption ages. The resulting eruption ages for the EC volcanic deposits range from 99.7 +1.3/-8.2 ka to 93.9 +5.9/-19.3 ka, overlapping within analytical uncertainties (Table 1).

The oldest deposits in this explosive-effusive sequence, the lower pumice, marks a maximum age for the volcanic eruption which, based on the ZDD eruption age of 93.9 +5.9/-19.3 ka, is coeval with a feldspar ^{40}Ar/^{39}Ar age for a lava flow cropping out ~2 km to the southeast of EC (89 ±18 ka; Preece et al., 2021). Importantly, textural evidence for zircon in contact with melt in pumice and lava support a juvenile, rather than entrained, origin for at least a proportion of the crystals in the magmatic system. Uniform zircon ^{238}U–^{230}Th isochron ages that overlap within uncertainty with, or at most ca. 13 kyr older than, the ZDD eruption ages reflect tapping of a common magma system.

The consistent relation between the ZDD eruption ages and the ^{238}U–^{230}Th crystallisation ages provides a first-order test for accuracy, because the former cannot predate the latter (Danišík et al., 2017). There is, however, an alternative age model for the post-dome lava breccia and orange-brown pumice eruptions of the EC sequence if validity is placed on the minority, two younger crystals, that were excluded from the above calculations of crystallisation ages. In this case, the lava breccia and orange-brown pumice deposits could have erupted as young as, respectively, ca. 60 ka and 50 ka; comparable in age to the aforementioned nearby Devil's Cauldron deposits, ca. 60 ka (Preece et al., 2021), and the Weather Post dome and rhyolite ~3 km southwest of EC dated at 54±2 and 52±3 ka (Jicha et al., 2013). Transient heating of zircon can result in partial or complete resetting of (U-Th)/He systematics. This effect was detected, for example, in 5–10 cm metasedimentary xenolith clasts preserved in a scoria fall deposit from Çakallar volcano, Turkey (Ulusoy et al., 2019). Pyrometamorphism of two clasts by basaltic magma resulted in a broad spread, tens to hundreds of ka, in the (U-Th)/He dates whereas zircon from a comparable xenolith considered to be completely reset yielded a much more restricted range consistent with, and having similar uncertainties to, cosmogenic ages of 4.7±1.2 ka (Ulusoy et al., 2019). By analogy, the main ca. 95 ka zircon (U-Th)/He age population, along with two older ca. 180 ka crystals in orange-brown pumice could have been derived from older disaggregated lithic clasts, not heated intensely enough in the effusive-explosive upper sequence regime to drive out any accumulated He. However, the (U-Th)/He age homogeneity in the essentially bimodal EC zircon population, albeit heavily skewed to ca. 95 ka, is inconsistent with He loss from older crystals that would be expected in a brief heating event (cf., Ulusoy et al., 2019).

Textural evidence also leads us to infer that incomplete resetting was not the main process controlling the upper EC sequence zircon eruption age distributions. Crystals are in contact with pumice glass and lava groundmass representing former melt, which would have resulted in effective heat transfer. In addition, the main zircon population is coeval with tiny acicular euhedral grains interpreted to have crystallised shortly before eruption. Thus, we conclude it is unlikely a significant eruptive hiatus is indicated after the ca. 95 ka cone pumice and dome emplacement by: the three young, ca. 41–52 ka (U-Th)/He dates from the stratigraphically highest deposits; and the youngest outlier, ca. 57 ka (U-Th)/He date, from the lava breccia. The complete EC sequence shows depositional continuity and mineralogical similarities, e.g., distinctive crystals of albite–anorthoclase feldspar (Davies et al., 2021). Furthermore, the dominant zircon population in the lava and orange-brown pumice consistently indicates ZDD eruption ages that are indistinguishable from the dome and underlying cone pumices emplacement. While the origin of the crystals yielding young (U-Th)/He dates and crystallisation ages remains unresolved, we suggest that the composite multi-clast pumice and lava breccia deposits sampled for this study may have been naturally contaminated by fall out or windblown ash emitted by younger eruptions either on Ascension Island or from an external source.

5.2 Insights into magmatic system evolution from zircon thermometry: saturation and crystallisation temperatures

5.2.1 Thermometry

The ZSTs are higher in the nearly aphyric lower and middle pumice than the more crystal-rich lava and orange-brown pumice. These differences are, most likely, an artefact of temperatures calculated with whole-rock rather than melt compositions, whereby actual melt Zr abundances are underestimated due to the presence of Zr-poor crystals leading to an underestimation of the real saturation temperature (Harrison et al., 2007). This highlights the problem of using ZST with whole-rock data, limiting the utility of the parameter to glassy volcanic rocks. Accordingly, the pumice ZST, 920°C, corresponds to the average calculated Ti-in-zircon crystallisation temperature, 930°C (range 850–1020°C), other crystallisation temperatures are below the ZST, consistent with the presence of zircon crystals in the samples.

The Ti-in-zircon thermometry average crystallisation temperature of 930°C is higher than the EC Fe-Ti oxide temperature of 855°C (Davies, 2021) but in the range of alkali feldspar-melt thermometry on EC low-K anorthoclase calculated at 250 MPa (9 km) in Thermobar (Wieser et al., 2021), by Davies (2021) using equation 24b from Putirka (2008) with microlite-melt pairs yielding 745–1046°C (H_2O 2.46–5.79 wt %). Our new temperatures also overlap with plagioclase-melt thermometry temperatures calculated for microlite- and macrocryst-melt pairs by Davies (2021) using equation 23 of Putirka (2008) in Thermobar (Wieser et al., 2021): microlite-melt 1014–1067°C (H_2O -0.95 – 2.77 wt %) and micro/macrocryst-melt 968–1069°C (H_2O -0.27–4.89 wt %). No crystallisation pressures were calculated in the current work, but Davies (2021) estimated minimum depth of ~8.5 km for crystallisation of EC magmas from H_2O contents of alkali-feldspar macrocrysts. Furthermore, from comparison with melt inclusion entrapment pressures and best fit fractional crystallisation modelling of zoned, mingled and island-wide fall deposits (Chamberlain et al, 2016; 2019; 2020) it may be inferred the parental magma originally ascended from <11 km.

The high temperatures obtained for the zircon crystallisation are consistent with an initially relatively dry magma (Kar et al., 1998). Some grains are entrained as inclusions in macrocrysts; however, as noted above zircon is also present in the pumice glass and lava groundmass consistent with it recording isotope and element concentrations in the melt at the time of crystallisation (see section '5.3.2 Zircon O isotopes - source character' below for discussion).

5.3 Insights into magmatic system evolution from whole-rock compositions and zircon mineral chemistry: tectonomagmatic context, source character and system processes

5.3.1 Zircon trace elements - tectonomagmatic context

Zircon trace elements are reliable indices for the tectonomagmatic conditions under which it crystallised (e.g., Grimes et al. 2015). Ascension Island formed in an oceanic intraplate setting, ~100 km west of the Mid-Atlantic Ridge and 50 km south of the Ascension Fracture Zone. Nonetheless, as noted above, uncertainty exists whether the magmatism originated from a low flux, shallow plume (Gaherty and Dunn, 2007) or anomalously enriched MORB (Paulick et al., 2010). Likewise, in a plot of U/Yb vs Hf (Fig. 4D; Grimes et al., 2015), from which tectonomagmatic setting may be inferred, the dome zircon straddle fields for high U/Yb of 'crustal input or enriched mantle source' and the low U/Yb N-MORB source; plotting in a region of overlap between the Iceland and Hawaii hotspots as well as island arcs. The lower pumice extends to higher Hf, more fractionated, compositions. Significantly more useful for discrimination is Sc/Yb which divides continental and arc derivation from oceanic sources and Nb/Yb that fingerprints an enriched component relative to typical MORB (Fig. 4E). Unexpectedly, the EC zircon fall in the 'continental and arc' field based on their Sc/Yb, but we suggest this ratio may be skewed to high Sc values by the absence of amphibole fractionation from the magma that crystallised the zircon. On the other hand, clear, uniformly high Nb/Yb in both the dome and lower pumice zircon, for which the relative immobility of Nb rules out the possibility of enrichment by seawater alteration, indicate involvement of an enriched component.

5.3.2 Zircon O isotopes - source character

Ascension Island whole-rock evolved lava and granite $\delta^{18}O$ values as low as 4.4‰, i.e., below mantle values, have been explained by sea or meteoric water infiltration into shallow rocks resulting from caldera subsidence followed by stoping and assimilation of these lithologies by the residual magma (Sheppard and Harris, 1985), or by assimilation of high-temperature altered oceanic crust (Weis et al., 1987). Zircon $\delta^{18}O$ values also range from mantle to sub-mantle compositions in both the EC dome and lower pumice (Fig. 4A). This is consistent magma derived from the same mantle source with heterogeneity resulting from variable assimilation of high-T, >300 °C hydrothermally alteration country rock prior to zircon crystallisation (cf., Adams, 1996; Bindeman and Valley, 2001; Carley et al., 2014; Jo et al., 2016; Scarrow et al., 2002). Latent heat of crystallisation may have facilitated assimilation as its effect is more evident in the evolved lower pumice that represents the top of the magma system (Fig. 4A) (cf., Thompson et al., 2002). Changes in magma volatile content may result in relatively oxidising conditions, as recorded in the positive EC zircon Ce/Ce* anomalies (Fig. 4C) (e.g., Kelley and Cottrell, 2009). Negative Eu/Eu* anomalies in all EC zircons are consistent with prior plagioclase crystallisation (Trail et al., 2012). Melt Ce content, on the other hand, is not affected by crystallisation of any major mineral, so anomalies may be considered a more dependable indication of oxidation state. Thus, the oxidizing conditions recorded by EC zircon (ΔFMQ +1.38 to +3.77) imply involvement of surface fluids, seawater or meteoric water.

Ascension Island mafic–felsic whole-rock $^{143}Nd/^{144}Nd$ values are uniformly high (0.5129–0.5131), whereas whole-rock $^{87}Sr/^{86}Sr$ values are more primitive for the mafic rocks (<0.703) than felsic ones (>0.704) (Weaver et al., 1996; Kar et al., 1998; Paulick et al., 2010). These data have been interpreted as the result of either post-emplacement alteration or low-degree assimilation of hydrothermally altered lithologies affecting the more evolved magmas (Kar et al., 1998). The new zircon O isotope data presented here resolve this conundrum because the low $\delta^{18}O$ component must have been present in the magma prior to zircon crystallisation; this is consistent with the noted lack of correlation of $\delta^{18}O$ with differentiation or age. Furthermore, the same assimilation process apparently affected the source magma for explosive lower pumice and the endogenous effusive dome indicative of it being a primary characteristic of the magma system. Extensive fracture permeability promotes efficient hydrothermal alteration of country rock at high temperatures, thus imprinting a low-$\delta^{18}O$ signature that is typical for hot spot and rift tectonomagmatic settings as well as nested caldera complexes (e.g., Troch et al., 2020; Scarrow et al., 2022). Notably, whole-rock major and trace element compositions do not usually reveal assimilation of co-genetic hydrothermally altered rock but this process can be detected in zircon $\delta^{18}O$ (Troch et al., 2020).

5.3.3 Zircon trace elements and whole-rock compositions - fractional crystallisation

The EC zircon chondrite-normalised REE patterns being parallel-subparallel in both samples are indicative, in agreement with the O isotope compositions, of crystallisation from magmas with a common source. On the other hand, the range in zircon Zr/Hf reflects progressive melt differentiation. The lower pumice zircon records more evolved compositions indicated by lower Zr/Hf than the dome zircon, which is consistent with the variation in whole-rock compositions. The dome zircon has somewhat more heterogeneous trace element compositions than the lower pumice with the compositional variation in the upper sequence effusive deposits indicating limited interconnectedness in the magmatic system.

Before considering the zircon trace element compositions in detail it is important to note that EC whole-rock SiO_2 abundances decrease from 68 wt % for the most evolved lower pumice deposit at the base of the sequence to 64 wt % at the less evolved top. Moreover, all major elements, as well as Sr, Ba and Eu, correlate negatively with SiO_2, suggesting they fractionated from the magma as it evolved, whereas K_2O and other trace elements correlate positively, excluding fractionation of a K-rich mineral phase such as sanidine. More evolved lower sequence deposits have a negative Eu anomaly whereas this is absent in the less evolved deposits at the top of the sequence. Inverting this whole-rock compositional gradient reveals progressive evacuation of a zoned magma system that was more evolved at the top and less evolved at the base. Displacement of the orange-brown pumice and lithic clasts from the main fractionation trend is indicative of their derivation from a spatially or temporally different magma system, consistent with their distinct zircon ages. Lack of appropriate experimental data makes it notoriously difficult to model alkaline systems with MELTS (Ghiorso and Gualda, 2015). Nevertheless, the major and trace element whole-rock trends are consistent with fractionation of the observed macrocryst assemblage: albitic plagioclase feldspar and fayalitic olivine with minor amounts of Fe-Ti oxides, clinopyroxene and apatite. Least-squares modelling using Petrograph (Petrelli et al., 2005) indicated a comparable crystallising assemblage for the compositionally zoned fall deposit mentioned above (Chamberlain et al., 2016).

Crustal lithologies typically have whole-rock chondritic Zr/Hf ratios, i.e., ~35–40 (Ahrens and Erlank, 1969; Hoskin and Schaltegger, 2003). Fractionation of zircon from evolved rocks such as granites and rhyolites, tends to produce lower Zr/Hf values with segregation of other Zr-bearing major minerals, e.g., amphibole, clinopyroxene, and garnet, augmenting this effect, but to a lesser degree (Bea et al., 2006). High whole-rock Zr/Hf ratios are consistent with accumulation of zircon grains by, we suggest, inefficient segregation hindering crystal fractionation at all stages of EC magma differentiation (e.g., Claiborne et al., 2006); this effect may have been amplified by the absence of amphibole fractionation which could result from relatively shallow magma storage, and moderate water contents, 1–6 wt % (e.g., Kar et al., 1998; Chamberlain et al., 2016, 2019, 2020; Davies, 2021).

A simple relationship between zircon trace element concentrations and degree of fractional crystallisation would be expected for closed system evolution of a uniform melt, e.g., positive correlations between zircon-compatible elements, for example, U, Th, Y and REE, and the differentiation index Zr/Hf and negative correlations with zircon incompatible elements (Storm et al., 2012; Troch et al., 2018; Cisneros de León and Schmitt, 2019). In the EC lower pumice and dome Sc shows the clearest negative correlation with Zr/Hf indicating it was incompatible in zircon during crystallisation and also that amphibole was not crystallising as the magma differentiated (cf., Scarrow et al., 2022). Notably, amphibole has only been found in Ascension Island volcanic rocks as xenocrysts from disaggregated plutonic clasts (Harris, 1982).

Weaker, albeit statistically significant, negative correlations are observed between EC zircon Zr/Hf and Y as well as the MREE-HREE. However, expected positive correlations of Zr/Hf with zircon-compatible elements such as U and Th are not detected. Thus, apparently paradoxically, the lower pumice, with a more evolved whole-rock composition, contains zircon with higher concentrations of ostensibly zircon-compatible elements. This may be explained, however, by the increased compatibility these elements at lower temperatures typical for more evolved magmas (e.g., Storm et al., 2014; Troch et al., 2018; Scarrow et al., 2021). Zircon from both samples also display variable Eu/Eu* that may indicate differences in the degree of plagioclase fractionation. On a cautionary note, we suggest that zircon trace element results should be interpreted with care because of the possible influence of nanoscale inclusions. These affected the dome zircon Ti contents and lower pumice zircon P values (supplementary material, 'Zircon trace elements'). Exotic accessory phases, commonly found in alkaline rocks, have been detected in both the lower pumice and dome: baddeleyite and REE-rich monazite, chevkinite; as well as apatite in the latter. Constraining these effects is beyond the scope of the current work, but merits further investigation.

It is evident that zircon geochronological-compositional data can provide an informative independent control on timing of magma crystallisation and compositional evolution.

The differences in zircon Zr/Hf in the more evolved lower pumice and less evolved dome place compositional constrains on the crystal sources, implying long-lived compositional segregation as discrete magma batches in a static, non-convecting, magma system preceding explosive evacuation of the pumice, dome exhumation and lava effusion.

6. Petrogenetic model for the Echo Canyon magmatic plumbing system

Key questions raised above regard longevity of magma storage, source character and magma plumbing processes. By combining new zircon age, isotopic and trace element data, whole-rock geochemical and petrographic compositions with field observations, we construct a model for the evolution of the EC ocean island magmatic plumbing system. Key aspects of this model include (paragraph numbers refer to Fig. 9):

1. The presence of an enriched component in the EC mantle source is suggested by the combination of high zircon trace element concentrations relative to MORB and lack of evidence for a continental component in the zircon O isotope values. The latter are mantle-like and variably depleted by open system heterogeneous assimilation of high-T hydrothermally altered country rock before zircon crystallisation.

2. Recurrent evolved magmatism at EC at 1.34 Ma, 0.6 Ma and 95 ka was identified from U–Th–Pb dating of volcanic lithic clasts that crop out in the most explosive pumices of EC stratigraphy identified by Davies et al. (2021). These data indicate that felsic volcanism was more widespread in the early history of the eastern island than previously recognised.

3. Eruption ages of the EC explosive-effusive deposits converge at ca. 95 ka – cone lower pumice 99.7 +1.3/-8.2 ka, dome 96.6 +8.4/-9.2 ka, lava breccia 95.1 +6.8/-11.2 ka, and orange-brown pumice 93.9 +5.9/-19.3 ka - confirming the temporal connection of the explosive-effusive sequence. Pre-eruptive zircon crystallisation – cone lower pumices 108 +10/-9 ka and 113 +15/-14 ka; post-cone dome 111 +4/-4 ka, lava breccia 108 +2/-2 ka and orange-brown

pumice 98.5 +5.9/-5.6 ka – occurred over a more prolonged duration of ca. 10^3–10^4 a. Zircon storage likely occurred under magmatic conditions because textures indicate contact with the melt. This low-flux ocean island system (Chamberlain et al., 2020 and references therein) has zircon residence time scales one to two orders of magnitude shorter than found in many subduction-related transcrustal mush systems (e.g., Bachmann et al., 2007; Cisneros de León et al., 2021; Scarrow et al., 2021).

4. The observed mineral assemblage was apparently in equilibrium, from agreement between zircon saturation, Ti-in-zircon crystallisation and alkali feldspar-melt temperatures for the crystal-poor pumices. Fractionated zircon trace element compositions indicate melt storage in discrete, but chemically zoned lenses. The lack of textural evidence for zircon dissolution, i.e., predominantly euhedral morphology (cf., Scarrow et al., 2021; Friedrichs et al., 2020) in addition to the absence of zoning in major mineral phases, supports volatile overpressure rather that mafic magma recharge being the eruptive trigger.

5. Zircon recycling prior to eruption is indicated by small, but systematic differences between zircon crystallisation and eruption ages and the higher-than-chondrite whole-rock Zr/Hf values. Compositional stratification where early eruptions, lower pumice, tapped more evolved magmas than late eruptions, lava breccia, is reflected in both whole-rock compositions and zircon Zr/Hf ratios.

7. Implications

An understanding of past magmatic processes including mineral crystallisation is necessary to develop models of eruption periodicity which is crucial for evaluating future volcanic hazards and associated risks. In the EC rocks we identify the deposits of the most explosive phases in the tephrostratigraphic sequence as useful targets for sampling lithic clasts recycled from previous magmatic events to establish the cyclicity. The increased energy of the eruptive paroxysm has the most potential to mobilise material from the volcanic edifice. The eruptive chronostratigraphy, and thus potential associated hazard, of the EC explosive-effusive transition sequence was not previously well-constrained. The new zircon crystallisation ages provide previously unidentified indications that magmatic activity beneath EC may be recurrent and prolonged. Significantly, zircon apparently crystallised during periods of eruptive quiescence, indicating that melt presence at depth may be unrelated to eruptive events.

Differences in zircon compositions, despite broadly similar crystallisation ages, and whole-rock compositional variations reflect progressive tapping of deeper and temporally more heterogeneous regions of the system, with magma compositions potentially controlling eruptive style.

The joint geochemical-geochronological ZDD approach employed here provides important insights into magma system timescales and processes that cannot be obtained from whole-rock or major mineral phase chemistry alone. The ZDD zircon dating tracks temporal variation in mineral assemblages in a way that is not possible for other silicate minerals, but which should be borne in mind when interpreting the results of thermobarometric calculations. Crystal provenance and residence times may be deciphered and related to sub-volcanic melt distribution and the thermal structure of the crust to inform how hazards may be most efficiently monitored. For example, unrest over sub-volcanic mush regions may be expected to be geographically restricted and thus effectively detected by a limited number of localised seismometer(s) whereas cold fractured crust may deform at a broader, regional, scale necessitating tracking of deformation by a more widely distributed seismic network. The recurrence of volcanism at EC identified by zircon from pumice and lavas as well as accidental lithic clasts highlights the need for continued zircon-based geochronological research. This, in conjunction with field-petrological-geochemical study, will constrain the past eruptive timescales and thus potential future magmatic behaviour of Ascension Island explosive-effusive felsic volcanism permitting evaluation of related hazards and risk.

Acknowledgements

This project received funding from the European Union's Horizon 2020 research and innovation programme under the Marie Skłodowska-Curie grant agreement No. 749611 (JHS). The work was also financially supported by the Spanish grant CGL 2017-84469-P (JHS). Funding for open access charge: Universidad de Granada/CBUA. Alexander Varychev at the University of Heidelberg, Germany, is thanked for help with analytical work. Giovanni Zanchetta is thanked for efficient and positive editorial handling. We are obliged to two anonymous reviewers for the time and effort they took to help us improve the clarity and rigour of our interpretations. This is the IBERSIMS publication Nº: 105.

References

Adams, M.C., 1996. Chemistry of fluids from ascension #1, a deep geothermal well on Ascension Island, South Atlantic Ocean. Geothermics, 25, 561-579

Ahrens, L.H., Erlank, A.J., 1969. Hafnium. In K.H. Wedepohl, Ed., Handbook of Geochemistry, 2, 5, B–O. Springer

Albarede, F., Feraud, G., Kaneoka, I., Allegre, C. J., 1978. ^{39}Ar-^{40}Ar dating: The importance of K-feldspars on multi-mineral data of polyorogenic areas. The Journal of Geology, 86: 581–598. doi:10.1086/649726.

Bachmann O., Charlier B.L.A., Lowenstern J.B., 2007. Zircon crystallization and recycling in the magma chamber of the rhyolitic Kos Plateau Tuff (Aegean arc). Geology, 35: 73–76

Banik, T.J., Carley, T.L., Coble, M.A., Hanchar, J.M., Dodd, J.P., Casale, G.M., McGuire, S.P., 2021. Magmatic processes at Snæfell Volcano, Iceland, constrained by Zircon Ages, isotopes, and trace elements. Geochemistry, Geophysics, Geosystems, 22. doi:10.1029/2020gc009255

Bea, F., Montero, P., Ortega, M., 2006. A LA-ICP-MS evaluation of Zr reservoirs in common crustal rocks: Implications for Zr and Hf geochemistry, and zircon-forming processes. The Canadian Mineralogist, 44, 693–714

Bindeman, I.N., Valley, J.W., 2001. Low-δ18O rhyolites from Yellowstone: Magmatic evolution based on analyses of zircons and individual phenocrysts. Journal of Petrology, 42, 1491–1517

Bindeman, I., Gurenko, A., Carley, T., Miller, C., Martin, E., Sigmarsson, O., 2012. Silicic magma petrogenesis in Iceland by remelting of hydrothermally altered crust based on oxygen isotope diversity and disequilibria between zircon and magma with implications for MORB. Terra Nova, 24, 227–232. doi:10.1111/j.1365-3121.2012.01058.x

Bjerga, A., Stubseid, H.H., Pedersen, L.-E.R, Pedersen, R.B., 2022. Radiation damage allows identification of truly inherited zircon. Communications Earth and Environment, 3. doi:10.1038/s43247-022-00372-2

Boehnke, P., Watson, E.B., Trail, D., Harrison, T.M., Schmitt, A.K., 2013. Zircon saturation re-revisited. Chemical Geology, 351, 324–334

Bohrson, W.A., Spera, F.J., Heinonen, J.S., Brown, G.A. Scruggs, M.A., Adams, J.V., Takach, M.K., Zeff, G., Suikkanen, E., 2020. Diagnosing open-system magmatic processes using the Magma Chamber Simulator (MCS): part I—major elements and phase equilibria. Contributions to Mineralogy and Petrology, 175, 104. doi:10.1007/s00410-020-01722-z

Carley, T.L., Miller, C.F., Wooden, J.L., Bindeman, I.N., Barth, A.P., 2011. Zircon from historic eruptions in Iceland: Reconstructing storage and evolution of silicic magmas. Mineralogy and Petrology, 102, 135–161. doi:10.1007/s00710-011-0169-3

Carley, T.L., Miller, C.F., Wooden, J.L., Padilla, A.J., Schmitt, A.K., Economos, R.C., Bindeman, I.N., and Jordan, B.T., 2014. Iceland is not a magmatic analog for the Hadean: Evidence from the zircon record. Earth and Planetary Science Letters, 405, 85–97

Cisneros de León, A., Schmitt, A.K., 2019. Intrusive reawakening of El Chichón volcano prior to its Holocene eruptive hyperactivity. Journal of Volcanology and Geothermal Research, 377, 53–68

Cisneros de León, A., Schindlbeck-Belo, J., Kutterolf, S., Danišík, M., Schmitt, A., Freundt, A., Pérez, W., Harvey, J., Wang, K.L., Lee, H.Y., 2021. A history of violence: Magma incubation, timing and tephra distribution of the Los Chocoyos Supereruption (Atitlán Caldera, Guatemala). Journal of Quaternary Science, 36, 169–179. doi:10.1002/jqs.3265

Cisneros de León, A., Danišík, M., Schindlbeck-Belo, J.C., Kutterolf, S., Schmitt, A.K., Freundt, A., Kling, J., Wang, K.-L., Lee, H.-Y., 2023. Timing and recurrence intervals for voluminous silicic eruptions from Amatitlán Caldera (Guatemala). Quaternary Science Reviews, 301, 107935. doi:10.1016/j.quascirev.2022.107935

Chamberlain K.J., Barclay J., Preece K., Brown R.J., Davidson J.P., E.I.M.F., 2016. Origin and evolution of silicic magmas at ocean islands: perspectives from a zoned fall deposit on Ascension Island, South Atlantic. Journal of Volcanology and Geothermal Research, 327, 349–360. doi:10.1016/j.jvolgeores.2016.08.014

Chamberlain K.J., Barclay J., Preece K.J., Brown R.J., Davidson J.P., 2019. Lower crustal heterogeneity and fractional crystallization control evolution of small-volume magma batches at Ocean Island Volcanoes (Ascension Island, South Atlantic). Journal of Petrology, 60, 1489–1522. doi:10.1093/petrology/egz037

Chamberlain K.J., Barclay J., Preece K., Brown R., McIntosh I., E.I.M.F., 2020. Deep and disturbed: conditions for formation and eruption of a mingled rhyolite at Ascension Island south Atlantic. Volcanica, 3, 139–153. doi:10.30909/vol.03.01.139153

Cherniak, D.J. Watson, E.B., 2001. Pb diffusion in Zircon. Chemical Geology, 172, 5–24. doi:10.1016/s0009-2541(00)00233-3

Claiborne, L.L., Miller, C.F., Walker, B.A., Wooden, J.L., Mazdab, F.K., Bea, F., 2006. Tracking magmatic processes through Zr/Hf ratios in rocks and Hf and Ti zoning in zircons: An example from the Spirit Mountain batholith, Nevada. Mineralogical Magazine, 70, 517–543

Claiborne, L.L., Miller, C.F., Flanagan, D.M., Clynne, M.A., Wooden, J.L., 2010. Zircon reveals protracted magma storage and recycling beneath Mount St. Helens. Geology, 38, 1011–1014

Daly, R.A., 1925. The geology of Ascension Island. Proceedings of the American Academy of Arts and Sciences, 6, 3-80

Danišík, M., Schmitt, A.K., Stockli, D.F., Lovera, O.M., Dunkl, I., Evans, N.J., 2017. Application of combined U-Th-disequilibrium/U-Pb and (U-Th)/He zircon dating to tephrochronology. Quaternary Geochronology, 40, 23-32

Danišík, M., Lowe, D.J., Schmitt, A.K., Friedrichs, B., Hogg, A.G., Evans, N.J., 2020. Sub-millennial eruptive recurrence in the silicic Mangaone Subgroup tephra sequence, New Zealand, from Bayesian modelling of zircon double-dating and radiocarbon ages. Quaternary Science Reviews, 246, 106517

Davies, B.V., 2021. Critical Eruptive Controls of an Intra-plate Volcano: Ascension Island, South Atlantic. PhD thesis, University of East Anglia, United Kingdom

Davies, B.V., Brown, R.J., Barclay, J., Scarrow, J.H., Herd, R.A., 2021. Rapid eruptive transitions from low to high intensity explosions and effusive activity: insights from textural analysis of a small-volume trachytic eruption, Ascension Island, South Atlantic. Bulletin of Volcanology, 83, 58, doi:10.1007/s00445-021-01480-1

Dosseto, A., Turner, S.P., A., Van Orman, J., 2011. Timescales of magmatic processes: From core to atmosphere. Wiley-Blackwell, Chichester (UK)

Famin, V., Paquez, C., Danišík, M., Gardiner, N.J., Michon, L., Kirkland, C.L., Berthod, C., Friedrichs, B., Schmitt, A.K., Monié, P., 2022. Multitechnique geochronology of intrusive and explosive activity on Piton des Neiges Volcano, Réunion Island. Geochemistry, Geophysics, Geosystems, 23. doi:10.1029/2021gc010214

Ferriss, E. D. A., Essene, E. J., Becker, U., 2008. Computational study of the effect of pressure on the Ti-in-zircon geothermometer. European Journal of Mineralogy, 20, 745–755

Ferry, J.M., Watson, E.B., 2007. New thermodynamic models and revised calibrations for the Ti-in-zircon and Zr-in-rutile thermometers. Contributions to Mineralogy and Petrology, 154, 429–437

Friedrichs, B., Atıcı, G., Danišík, M., Atakay, E., Çobankaya, M., Harvey, J.C., Yurteri, E., Schmitt, A.K., 2020. Late Pleistocene eruptive recurrence in the post-collisional Mt. Hasan stratovolcanic complex (Central Anatolia) revealed by zircon double-dating. Journal of Volcanology and Geothermal Research 404, 107007. doi:10.1016/j.jvolgeores.2020.107007

Gaherty, J. B., Dunn, R.A., 2007. Evaluating hot spot–ridge interaction in the Atlantic from regional-scale seismic observations, Geochemistry Geophysics and Geosystems, 8, Q05006, doi:10.1029/2006GC001533

Ghiorso, M.S., Evans, B.W., 2008. Thermodynamics of rhombohedral oxide solid solutions and a revision of the Fe-Ti two-oxide geothermometer and oxygen-barometer. American Journal of Science, 3, 957–1039

Ghiorso, M.S., Gualda, G.A., 2015. An H2O–CO2 mixed fluid saturation model compatible with rhyolite-melts. Contributions to Mineralogy and Petrology, 169. doi:10.1007/s00410-015-1141-8

Greenough, J.D., Kamo, S.L., Davis, D.W., Larson, K., Zhang, Z., Layton-Matthews, D., De Vera, J., Bergquist, B.A., 2021. Old subcontinental mantle zircon below Oahu. Communications Earth Environment 2. doi:10.1038/s43247-021-00261-0

Grimes, C.B., Wooden, J.L., Cheadle, M.J., John, B.E., 2015. “Fingerprinting” tectono-magmatic provenance using trace elements in igneous zircon. Contributions to Mineralogy and Petrology, 170, 46. doi:10.1007/s00410-015-1199-3

Hanchar, J.M, Hoskin, P.W.O., 2003. Zircon. Reviews in Mineralogy and Geochemistry, 53, Mineralogical Society of America, Chantilly.

Harris, C., 1982. Coarse-grained rocks of Ascension Island. PhD thesis, University of Oxford, United Kingdom

Harris, C., 1983. The petrology of lavas and associated plutonic inclusions of Ascension Island. Journal of Petrology, 24:424–470. doi:10.1093/petrology/24.4.424

Harrison, T.M., Watson, E.B., Aikman, A.B., 2007. Temperature spectra of zircon crystallization in plutonic rocks. Geology, 35, 635–638

Hoskin, P.W.O., and Ireland, T.R., 2000. Rare earth element chemistry of zircon and its use as a provenance indicator. Geology, 28, 627–630

Hoskins, P.W.O., Schaltegger, U., 2003. The composition of zircon and igneous and metamorphic petrogenesis. In: Hanchar, J.M., Hoskins, P.W.O. (Eds.), Zircon. Reviews in Mineralogy and Geochemistry, 53, 27–62

Hughen, K.A., 2007. Radiocarbon Dating of Deep-Sea Sediments. In Hillaire–Marcel, C., De Vernal, A. (Eds.), Developments in Marine Geology, Elsevier.

Jicha, B.R., Singer, B.S., Valentine, M.J., 2013. ^{40}Ar/^{39}Ar geochronology of subaerial Ascension Island and a re-evaluation of the temporal progression of basaltic to rhyolitic volcanism. Journal of Petrology, 54, 2581–2596

Jo, H.J., Chang-Sik Cheong, A., Ryu, J.S., Kim, N., Yi, K., Jung, H. Li, X.H., 2016. In-situ oxygen isotope records of crustal self-cannibalization selectively captured by zircon crystals from high-δ26Mg granitoids. Geology, 44, 339–342

Kar, A. Weaver, B. Davidson, J. Colucci, M., 1998. Origin of differentiated volcanic and plutonic rocks from Ascension Island, South Atlantic Ocean. Journal of Petrology 39, 1009–1024. doi:10.1093/petroj/39.5.1009

Kelley, K.A., Cottrell, E., 2009. Water and the oxidation state of subduction zone magmas. Science, 325, 605–607

Klingelhofer, F., Minshull, T.A., Blackman, D.K., Harben, P., Childers, V., 2001. Crustal structure of Ascension Island from wide-angle seismic data: implications for the formation of near-ridge volcanic islands. Earth and Planetary Science Letters, 190, 41–56

Lanos P., Dufresne P., 2019. ChronoModel version 2.0 User manual. pp.84, https://ffhal02058018f.

Loucks, R.R., Fiorentini, M.L., Henríquez, G.J., 2020. New magmatic oxybarometer using trace elements in zircon. Journal of Petrology, 61. doi:10.1093/petrology/egaa034

Marsden, R.C., Danišík, M., San Ahn, U., Friedrichs, B., Schmitt, A.K., Kirkland, C.L., McDonald, B.J. Evans, N.J., 2021. Zircon double-dating of Quaternary eruptions on Jeju Island, South Korea. Journal of Volcanology and Geothermal Research, 410, 107171

McDonough, W.F., Sun S.-S., 1995. The composition of the Earth. Chemical Geology, 120, 223-253

Ni, Z., Arevalo, R., Piccoli, P., Reno, B.L., 2020. A novel approach to identifying mantle-equilibrated zircon by using trace element chemistry. Geochemistry, Geophysics, Geosystems, 21, e2020GC009230.

Paces, J.B., Miller, J.D., 1993. Precise U-Pb ages of Duluth Complex and related mafic intrusions, northeastern Minnesota: Geochronological Insights to physical, petrogenetic, paleomagnetic, and tectonomagmatic processes associated with the 1.1 Ga midcontinent rift system. Journal of Geophysical Research: Solid Earth 98, 13997–14013. doi:10.1029/93jb01159

Padilla, A.J., Miller, C.F., Carley, T.L., Economos, R.C., Schmitt, A.K., Coble, M.A., Wooden, J.L., Fisher, C.M., Vervoort, J.D., Hanchar, J. M., 2016. Elucidating the magmatic history of the Austurhorn silicic intrusive complex (Southeast Iceland) using zircon elemental and isotopic geochemistry and geochronology. Contributions to Mineralogy and Petrology, 171, 1–21.

Paulick H., Münker C., Schuth S., 2010. The influence of small-scale mantle heterogeneities on Mid-Ocean Ridge volcanism: Evidence from the southern Mid-Atlantic Ridge (7°30'S to 11°30'S) and Ascension Island. Earth and Planetary Science Letters, 296, 299-310.

Petrelli, M., Poli, G., Perugini, D., Peccerillo, A., 2005. PetroGraph: a new software to visualize, model, and present geochemical data in igneous petrology. Geochemistry Geophysics and Geosystems, 6. doi:10.1029/2005gc000932

Preece, K., Mark, D.F., Barclay, J., Cohen, B.E., Chamberlain, K.J., Jowitt, C., Vye-Brown, C., Brown, R.J., Hamilton, S., 2018. Bridging the gap: $^{40}Ar/^{39}Ar$ dating of volcanic eruptions from the 'age of Discovery'. 'Geology 46, 1035–1038. doi:10.1130/g45415.1

Preece, K.J. Barclay, J. Brown, R.J. Chamberlain, K.J. Mark, D.F., 2021. Explosive felsic eruptions on ocean islands: a case study from Ascension Island (South Atlantic). Journal of Volcanology and Geothermal Research, 416. doi:10.1016/j.jvolgeores.2021.107284

Putirka, K.D., 2008. 3. Thermometers and barometers for volcanic systems. Minerals, inclusions and volcanic processes 61–120. doi:10.1515/9781501508486-004

Reiners, P.W., Spell, T.L., Nicolescu, S. and Zanetti, K.A., 2004. Zircon (U-Th)/He thermochronometry: He diffusion and comparisons with 40Ar/39Ar dating. Geochimica et Cosmochimica Acta, 68, 1857-1887.

Rojas-Agramonte, Y., Kaus, B.J., Piccolo, A., Williams, I.S., Gerdes, A., Wong, J., Xie, H.X., Buhre, S., Toulkeridis, T., Montero, P., Garcia-Casco, A., 2022. Zircon dates long-lived plume dynamics in Oceanic Islands. Geochemistry, Geophysics, Geosystems, 23. doi:10.1029/2022gc010485

Rolim, J.M., 2022. First U-Pb age constraints from plutonic xenoliths preserved in alkaline volcanic rocks of the Brazilian Fernando de Noronha Archipelago, Southwest Atlantic Ocean. Masters thesis, Universidade Federal de Minas Gerais, Brazil

Sagan, M., Heaman, L.M., Pearson, D.G., Luo, Y., Stern, R.A., 2020. Removal of continental lithosphere beneath the Canary archipelago revealed from a U-Pb age and Hf/O isotope study of modern sand detrital zircons. Lithos, 362-363, 105448. doi:10.1016/j.lithos.2020.105448

Scarrow J.H., Schmitt A.K., Barclay J., Horstwood M.S.A., Bloore A.J. Christopher T.E., 2021. Zircon as a tracer of plumbing processes in an active magmatic system: insights from mingled magmas of the 2010 dome collapse, Montserrat, Lesser Antilles Arc, Caribbean. Journal of Volcanology and Geothermal Research, 420, 107390. doi:10.1016/j.jvolgeores.2021.107390

Scarrow J.H., Chamberlain K.J., Montero P., Horstwood M.S.A., Kimura J.-I., Tamura Y., Chang Q., Barclay J., 2022. Zircon geochronological and geochemical insights into pluton building and volcanic-hypabyssal-plutonic connections: Oki-Dōzen, Sea of Japan—A complex intraplate alkaline volcano. American Mineralogist, 107, 1545–1562. doi:10.2138/am-2021-7861

Schaltegger, U., Schmitt, A.K., Horstwood, M.S.A., 2015. U–Th–Pb zircon geochronology by ID-TIMS, SIMS, and laser ablation ICP-MS: Recipes, interpretations, and opportunities. Chemical Geology, 402, 89-110. doi: 10.1016/j.chemgeo.2015.02.028.

Schmitt, A.K., Stockli, D.F. and Hausback, B.P., 2006. Eruption and magma crystallization ages of Las Tres Vírgenes (Baja California) constrained by combined 230Th/238U and (U–Th)/He dating of zircon. Journal of Volcanology and Geothermal Research, 158, 281-295

Shao, T., Xia, Y., Ding, X., Cai, Y., Song, M., 2019. Zircon saturation in terrestrial basaltic melts and its geological implications. Solid Earth Sciences, 4, 27–42. doi:10.1016/j.sesci.2018.08.001

Sheppard, S.M., Harris, C., 1985. Hydrogen and oxygen isotope geochemistry of Ascension Island Lavas and granites: Variation with crystal fractionation and interaction with sea water. Contributions to Mineralogy and Petrology, 91, 74–81. doi:10.1007/bf00429429

Smythe, D.J., Brenan J.M., 2015. Cerium oxidation state in silicate melts: combined fO2 temperature and compositional effects. Geochimica Cosmochimica Acta, 170, 173–187

Storm, S., Shane, P., Schmitt, A.K., Lindsay, J.M., 2012. Decoupled crystallization and eruption histories of the rhyolite magmatic system at Tarawera volcano revealed by zircon ages and growth rates. Contributions to Mineralogy and Petrology, 163, 505–519

Storm, S., Schmitt, A.K., Shane, P., and Lindsay, J.M., 2014. Zircon trace element chemistry at sub-micrometer resolution for Tarawera volcano, New Zealand, and implications for rhyolite magma evolution. Contributions to Mineralogy and Petrology, 167, 1–19.

Thompson, A., Matile, L., Ulmer, P., 2002. Some thermal constraints on crustal assimilation during fractionation of hydrous, mantle-derived magmas with examples from central Alpine batholiths. Journal of Petrology, 43, 403–422. doi:10.1093/petrology/43.3.403

Trail, D., Watson, B.E., Tailby, N.D., 2012. Ce and Eu anomalies in zircon as proxies for the oxidation state of magmas. Geochimica Cosmochimica Acta, 97, 70–87

Torsvik, T.H., Amundsen, H., Hartz, E.H., Corfu, F., Kusznir, N., Gaina, C., Doubrovine, P.V., Steinberger, B., Ashwal, L.D., Jamtveit, B., 2013. A Precambrian microcontinent in the Indian Ocean. Nature Geoscience, 6, 223–227. doi:10.1038/ngeo1736

Troch, J., Ellis, B.S., Schmitt, A.K., Bouvier, A.S., Bachmann, O., 2018. The dark side of zircon: textural, age, oxygen isotopic and trace element evidence of fluid saturation in the subvolcanic reservoir of the Island Park-Mount Jackson Rhyolite, Yellowstone (USA). Contributions to Mineralogy and Petrology,173, 1–17.

Troch, J., Ellis, B.S., Harris, C., Bachmann, O., and Bindeman, I.N., 2020. Low-δ^{18}O silicic magmas on Earth: A review. Earth Science Reviews, 208, 103299

Ulusoy, İ., Sarıkaya, M.A., Schmitt, A.K., şen, E., Danišík, M., Gümüş, E., 2019. Volcanic eruption eye-witnessed and recorded by prehistoric humans. Quaternary Science Reviews, 212, 187–198. doi:10.1016/j.quascirev.2019.03.030

Valley, J.W., 2003. Oxygen isotopes in zircon. Reviews in Mineralogy and Geochemistry, 53, 343–385.

Vazquez, J.A., Shamberger, P.J., Hammer, J.E., 2007. Plutonic xenoliths reveal the timing of magma evolution at Hualalai and Mauna Kea, Hawaii. Geology, 35, 695. doi:10.1130/g23495a.1

Watson, E.B., Harrison, T.M., 1983. Zircon saturation revisited: temperature and composition effects in a variety of crustal magma types. Earth and Planetary Science Letters, 64, 295–304

Weaver B., Kar A., Davidson J., Colucci M., 1996. Geochemical characteristics of volcanic rocks from Ascension Island, South Atlantic Ocean. Geothermics, 25, 449–470

Weis, D., Demaiffe, D., Cauet, S., Javoy, M., 1987. Sr, Nd, O and H isotopic ratios in Ascension Island lavas and plutonic inclusions; cogenetic origin. Earth and Planetary Science Letters, 82, 255–268. doi:10.1016/0012-821x(87)90200-7

Wiedenbeck, M., All e, P., Corfu, F., Griffin, W.L., Meier, M., Oberli, F., Quadt, A.V., Roddick, J.C., Spiegel, W., 1995. Three Natural Zircon Standards for U-Th-Pb, Lu-Hf, Trace Element and REE analyses. Geostandards Newsleter, 19, 1–23

Wieser, P. Petrelli, M. Lubbers, J. Wieser, E. Kent, A. Till, C., 2021. Thermobar: A critical evaluation of mineral-melt thermobarometry and hygrometry in arc magmas using a new open-source Python3 tool. Geological Society of America Abstracts with Programs, 53, 6, doi:10.1130/abs/2021AM-367080

Figure captions

Figure 1

Simplified geological map of Ascension Island, adapted from Chamberlain et al. (2016) showing distribution of mafic and felsic effusive and explosive products, and key infrastructure locations. 1 Georgetown, 2 Two Boats Village, 3 Travellers Hill Royal Air Force station, 4 US air force base, 5 Wideawake Airfield. Asterisk marks the location of Echo Canyon and cross the youngest basaltic lava flows. Inset: Location of Ascension Island relative to the Mid-Atlantic Ridge in the South Atlantic.

Figure 2

Composite stratigraphic log of the Echo Canyon (EC) section. Dashed grey horizontal lines mark the contact between explosive and effusive deposits. Clast types and key bed characteristics are detailed in the key. Sample numbers indicated to the right of each unit.

Figure 3

Whole-rock major and trace element data pumice and lavas from the Echo Canyon (EC) deposits. Analytical uncertainty is less than symbol size. A. Total alkalis vs silica diagram showing EC deposits plot in the trachyte field, except for one rhyolitic lithic clast; explosive pumices are more evolved than the dome, lava and orange-brown pumice. Alkaline (Alk) and calc-alkaline (Ca) plus tholeiitic (Th) fields indicated. Symbols are larger than analytical error. B. Trace elements normalised to chondrite showing pumices are depleted in Eu relative to the dome, lava and orange-brown pumice, normalisation values from McDonough and Sun (1995). C. MgO vs SiO_2. D. K_2O vs SiO_2. Note the orange-brown pumice lies off the trend defined by the dome, lava and pumices. Major elements expressed as wt % oxides. Comparative Ascension Island whole-rock data shown in A and B as a grey field (data from Weaver et al., 1996; Kar et al., 1998; Jicha et al., 2013; Chamberlain et al., 2019).

Figure 4

A. Zircon $\delta^{18}O$ values. The grey horizontal band marks the compositional range typical of zircon crystallised from mantle-derived magmas (Valley 2003). Note that values of $\delta^{18}O$ below 4.7 are typical of magmatic systems that assimilated a significant component of high temperature hydrothermally altered crust. The 2σ errors on the $\delta^{18}O$ values are within the symbol size; B. Zircon Sc concentration vs differentiation index Zr/Hf, symbols as in 4A, all trace elements expressed in ppm; C. Zircon chondrite-normalised rare earth element plots. All samples show parallel patterns with a pronounced positive anomaly in Ce and a negative anomaly in Eu. Normalisation values of McDonough and Sun (1995), symbols as in 4A; D. Zircon U/Yb vs Hf tectonomagmatic discrimination diagram of Grimes et al. (2015). The dome zircon plots in the enriched mantle source region of the overlapping Iceland and Hawaii fields;

the lower pumice zircon plot along a parental melt fractionation trend from the dome, symbols as in 4A; E. Zircon Sc/Yb vs Nb/Yb tectonomagmatic discrimination diagram of Grimes et al. (2015). All analysed zircon has relatively high Nb/Yb indicative of an enriched mantle source, whereas the unexpectedly high Sc/Yb for an ocean island setting is attributed to lack of amphibole fractionation, symbols as in 4A.

Figure 5

Echo Canyon ^{238}U–^{230}Th zircon crystallisation ages in isochron diagrams. Red solid line represents model isochron for the Bayesian eruption age estimates.

Figure 6

Echo Canyon U-Pb zircon crystallisation ages for lithic clasts in a Tera-Wasserburg isochron diagram. Isochron is drawn for a fixed intercept corresponding to anthropogenic common Pb on the surface of SIMS mounts, with ages derived from the concordia intercept accounting for disequilibrium (initial $^{230}Th/^{238}U = 0.2$, $^{231}Pa/^{235}U = 3$).

Figure 7

Rank order plots of α-ejection- and disequilibrium-corrected zircon (U-Th)/He dates displayed as 2σ error bars. Weighted mean (U-Th)/He age values and corresponding 95% confidence intervals are listed as numerals and displayed as solid black vertical lines through each population and outer dashed black lines. Red-pink bars indicate values considered for calculation of weighted mean for the main population; grey bars indicate statistical outliers identified by Isoplot 4.15 (Ludwig, 2012) based on a modified 2-sigma criterion.

Figure 8

Posterior distribution graphs for probability densities (curves) of the eruption ages predicted by Bayesian age sequence model in ChronoModel v. 2.0. The 95% highest posterior density (HDP) regions are represented by the horizontal bars above the curves and by the grey filled areas under the curves. Labels: name of the deposit; the mode of the posterior distribution (i.e., maximum *a posteriori* probability or 'MAP') in ka; 95% HPD in ka. Numerical results can be found in supplementary material 'Zircon double dating ages'.

Figure 9

Schematic representation of timing and processes in the magma system beneath Echo Canyon (EC). Key aspects are labelled with numbers relating to the "Petrogenetic model for the Echo Canyon magmatic plumbing system" section of the text. The crustal cross-section highlights mantle input, the depth of melt evolution and the proposed position of previous eruptive products relative to the EC stratigraphic sequence. Irregular vertical blue lines represent pathways for hydrothermal alteration. The magma system shows a variation in wt % SiO_2 with depth in the discrete magma lenses and zircon compositional and age ranges. The zoom lens shows zircon preserved both as inclusions in macrocrysts and in contact with the melt. Zircon colour composition and size age are schematic. The erupted EC stratigraphy summarises the inverse evacuation of the compositionally stratified magma system as alternating explosive and effusive eruptive deposits. Not to vertical scale.

Figure

Click here to access/download;Figure;EC_Fig. 1_revised.pdf

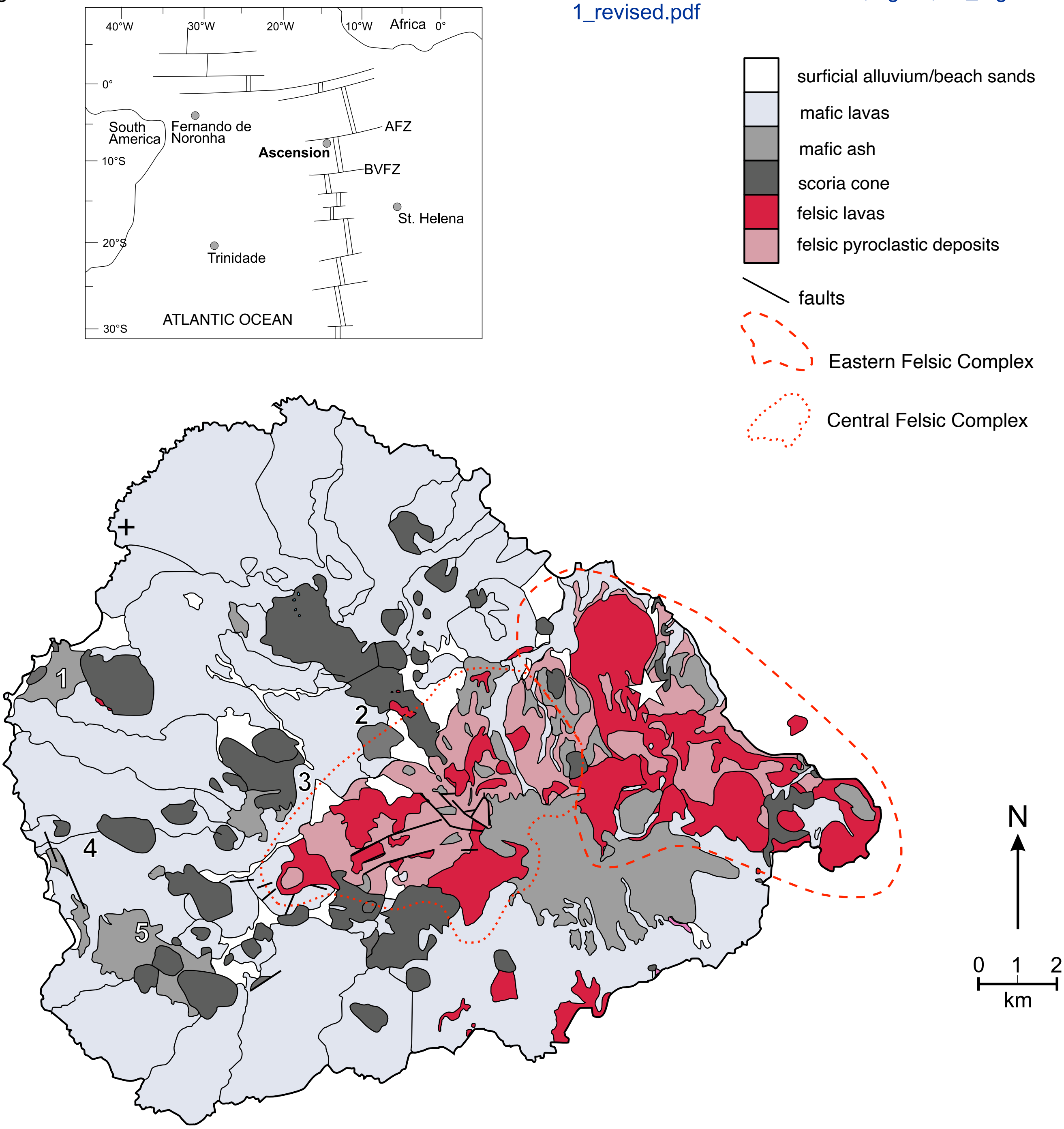

Figure

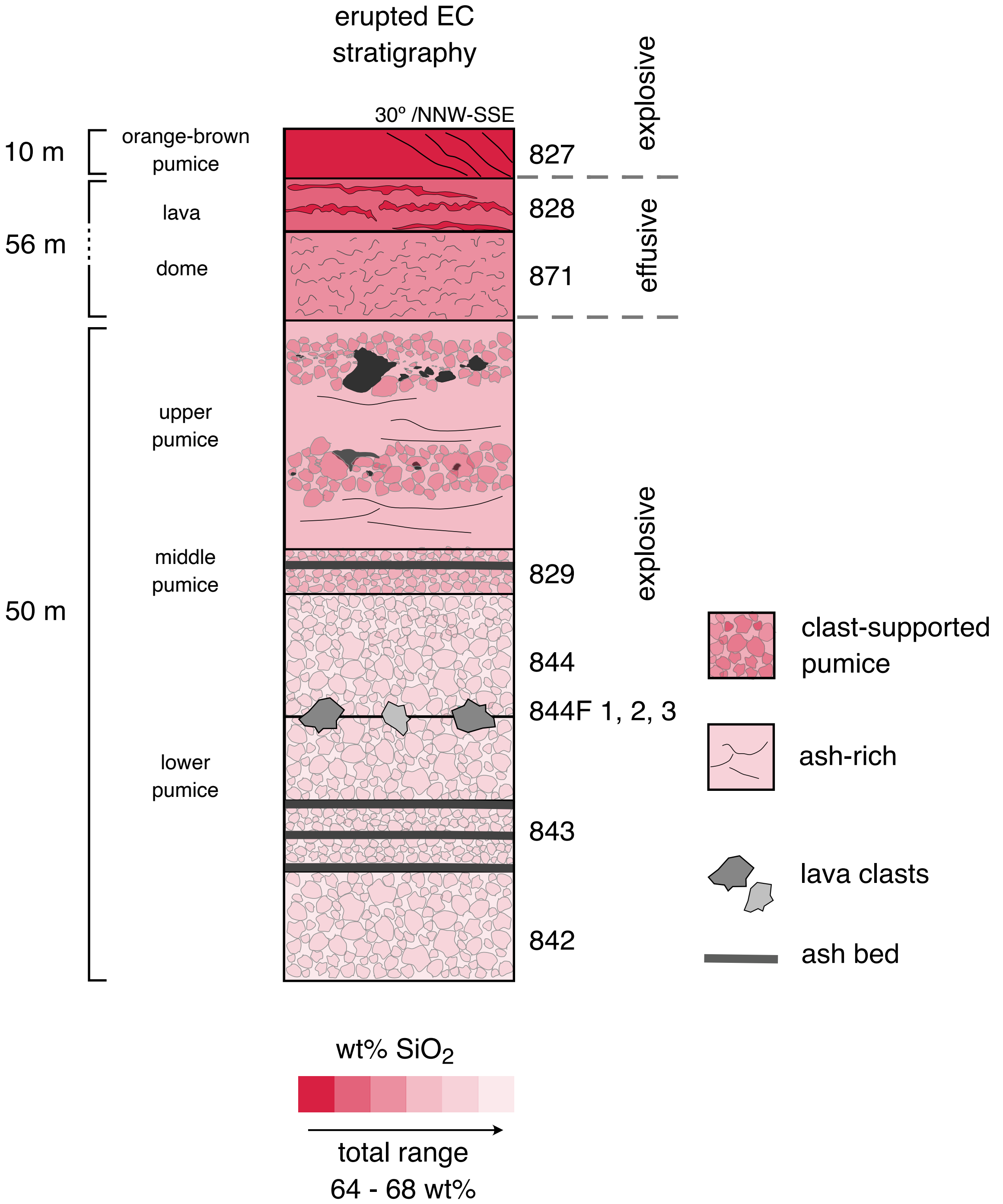

erupted EC
stratigraphy
30° /NNW-SSE
10 m
orange-brown
pumice
827
explosive
lava
828
56 m
dome
871
effusive
upper
pumice
middle
pumice
829
explosive
50 m
844
844F 1, 2, 3
lower
pumice
843
842
clast-supported
pumice
ash-rich
lava clasts
ash bed
wt% SiO_2
total range
64 - 68 wt%

Figure

Click here to access/download;Figure;EC_Fig. 3_revised.pdf

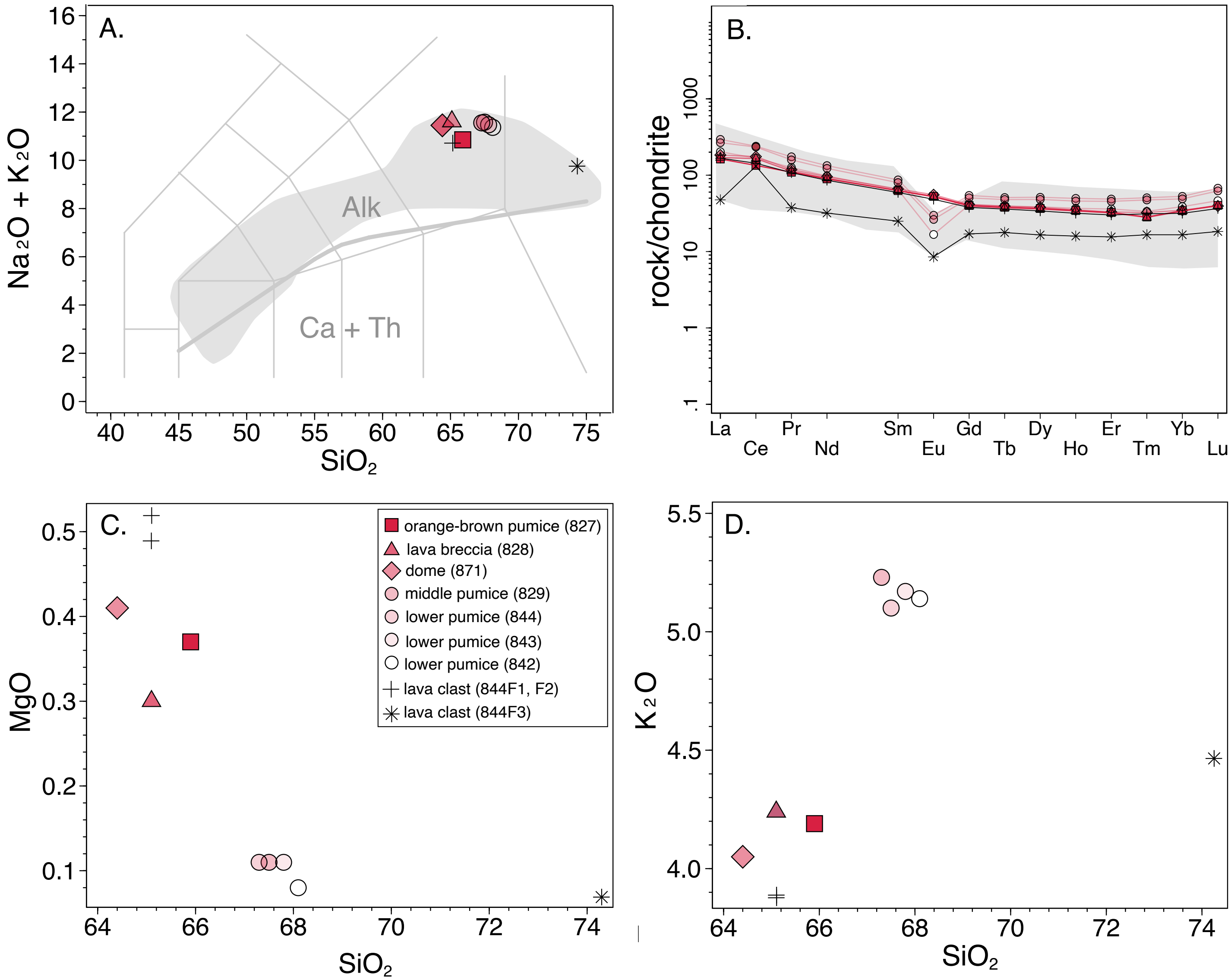

Figure

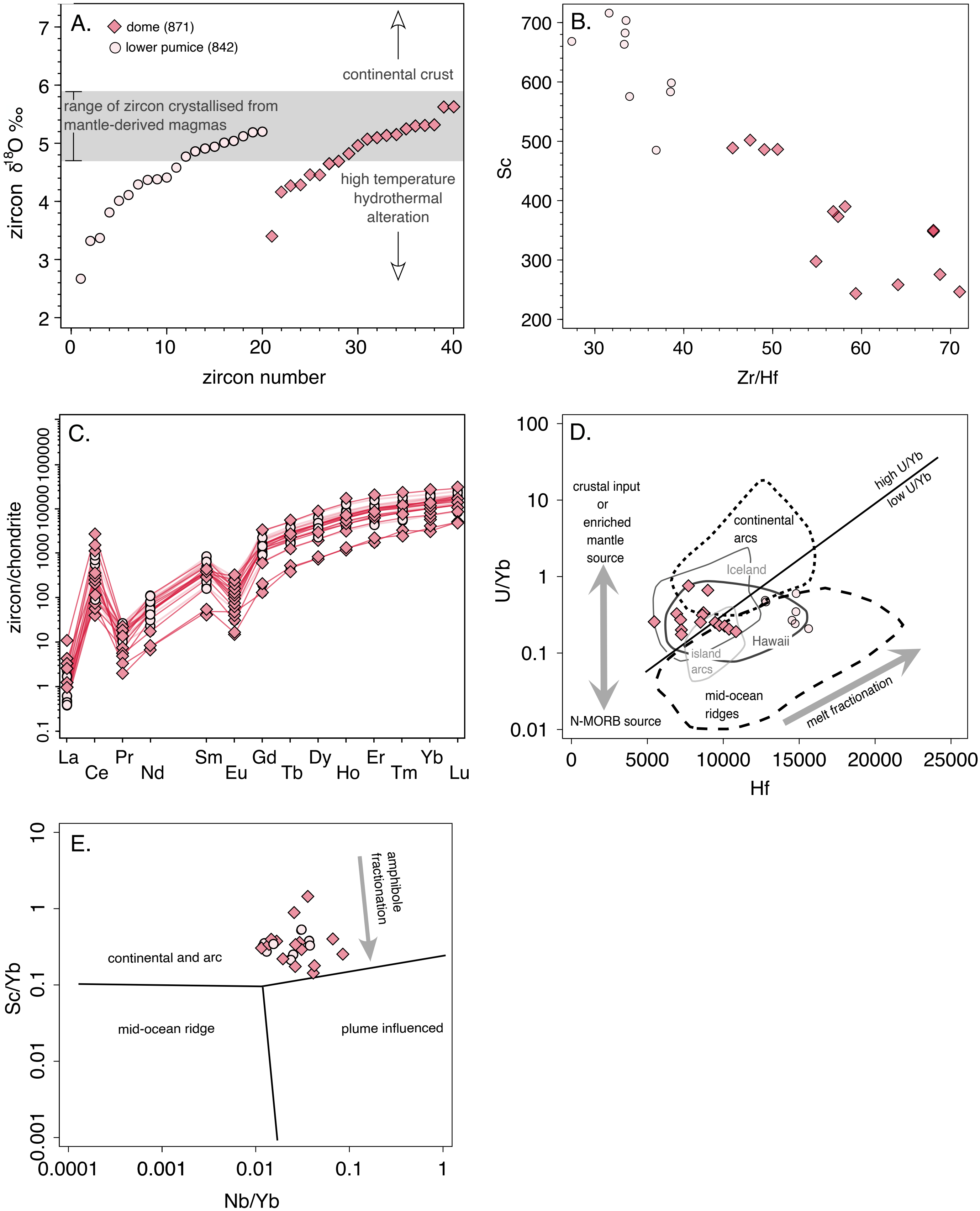

A.
dome (871)
lower pumice (842)
continental crust
range of zircon crystallised from mantle-derived magmas
high temperature hydrothermal alteration
zircon δ18O ‰
zircon number
B.
Sc
Zr/Hf
C.
zircon/chondrite
La Ce Pr Nd Sm Eu Gd Tb Dy Ho Er Tm Yb Lu
D.
crustal input or enriched mantle source
N-MORB source
continental arcs
Iceland
Hawaii
island arcs
mid-ocean ridges
high U/Yb
low U/Yb
melt fractionation
U/Yb
Hf
E.
amphibole fractionation
continental and arc
mid-ocean ridge
plume influenced
Sc/Yb
Nb/Yb

Figure

Click here to access/download;Figure;EC_Fig. 5_revised.pdf

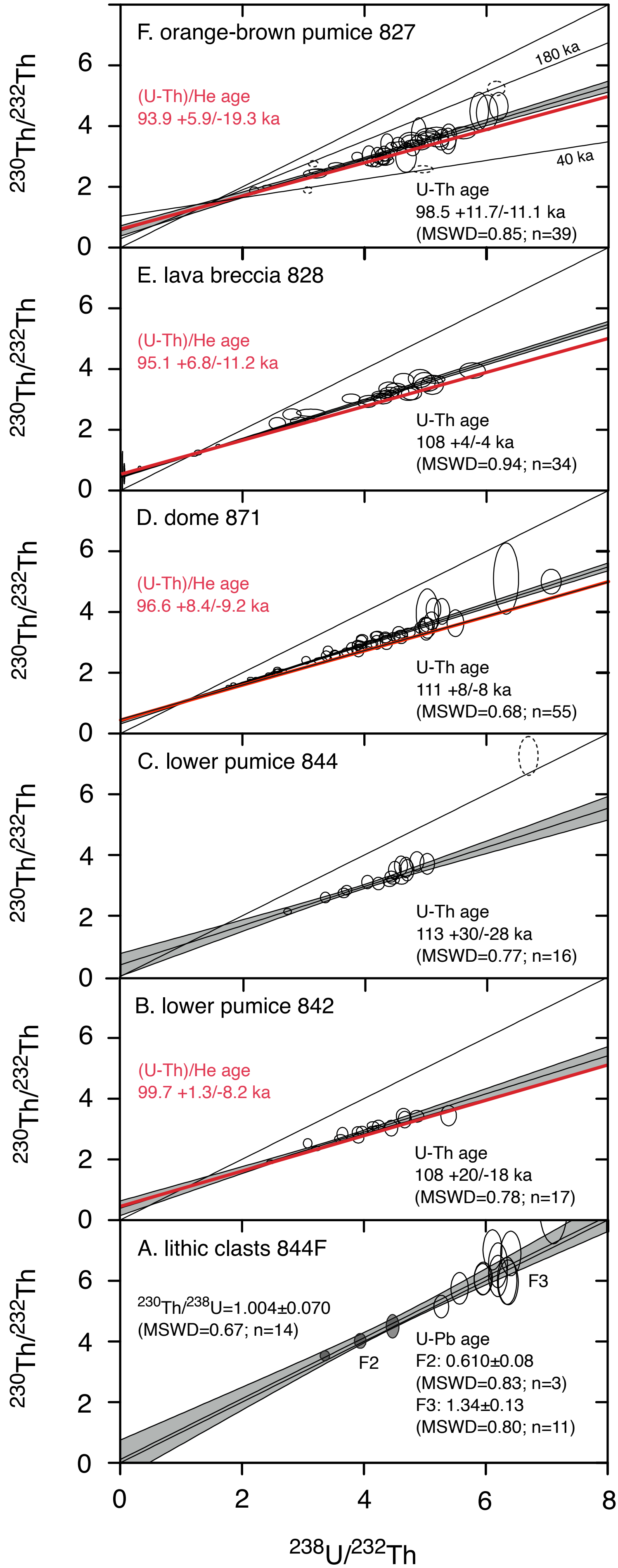

Figure

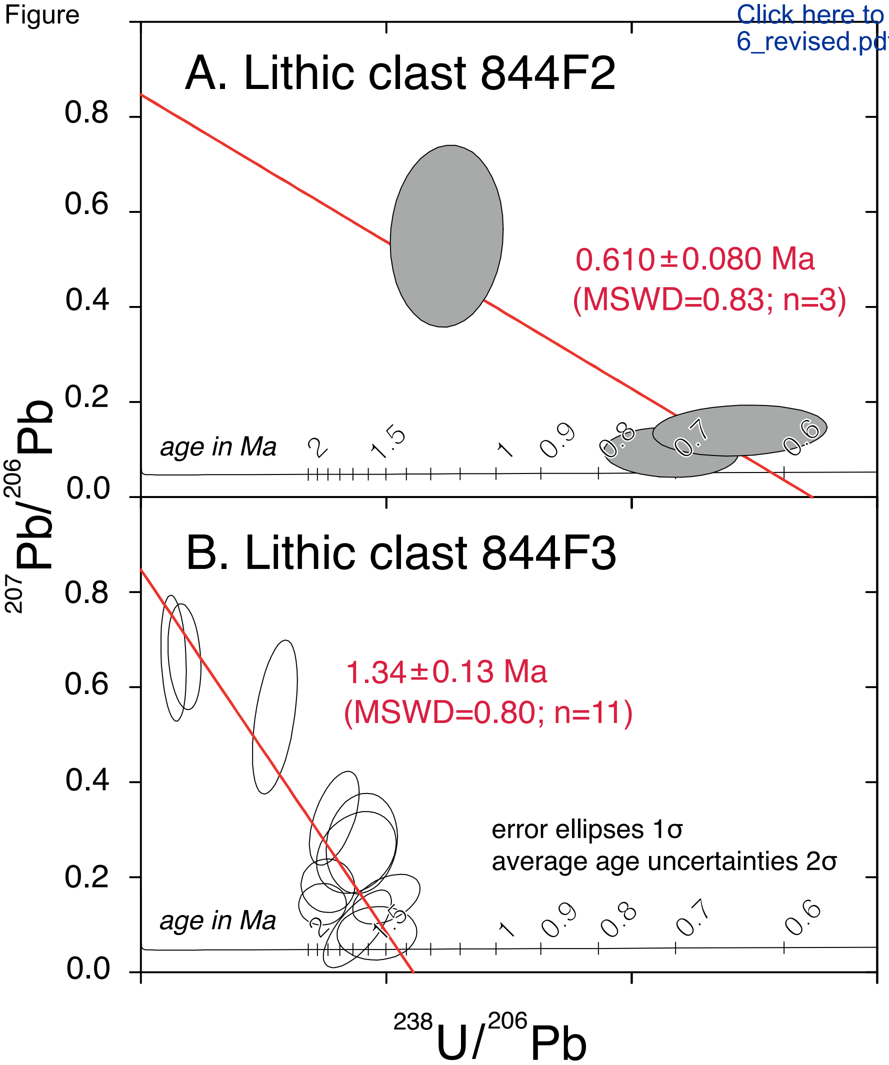

A. Lithic clast 844F2
0.610±0.080 Ma
(MSWD=0.83; n=3)
age in Ma
2
1.5
1
0.9
0.8
0.7
0.6
B. Lithic clast 844F3
1.34±0.13 Ma
(MSWD=0.80; n=11)
error ellipses 1σ
average age uncertainties 2σ
age in Ma
2
1.5
1
0.9
0.8
0.7
0.6
0.8
0.6
0.4
0.2
0.0
$^{207}Pb/^{206}Pb$
$^{238}U/^{206}Pb$

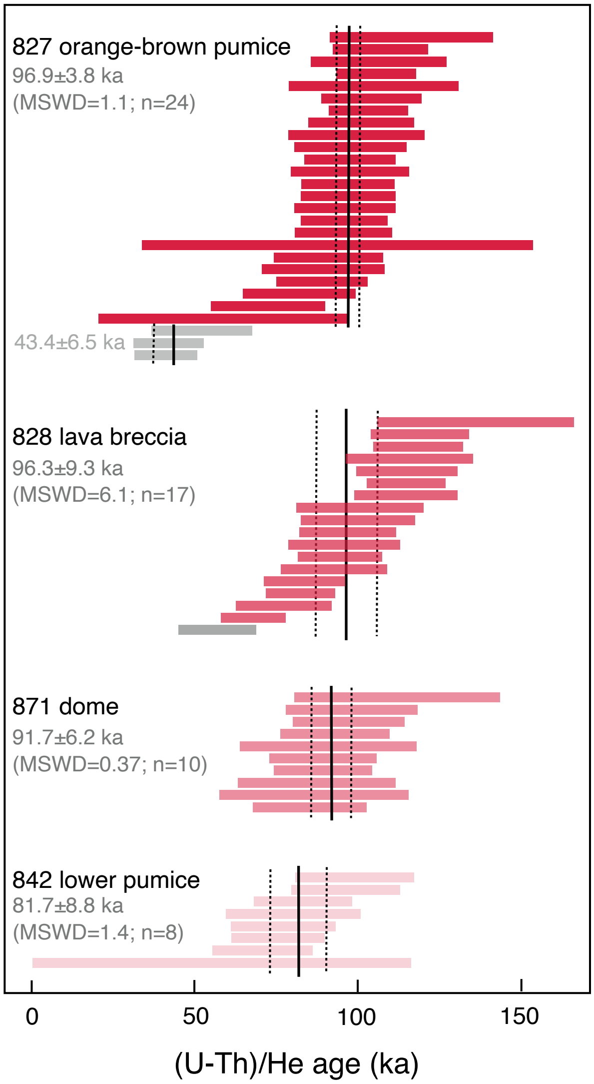
827 orange-brown pumice
96.9±3.8 ka
(MSWD=1.1; n=24)
43.4±6.5 ka
828 lava breccia
96.3±9.3 ka
(MSWD=6.1; n=17)
871 dome
91.7±6.2 ka
(MSWD=0.37; n=10)
842 lower pumice
81.7±8.8 ka
(MSWD=1.4; n=8)
0
50
100
150
(U-Th)/He age (ka)

Fig. 8

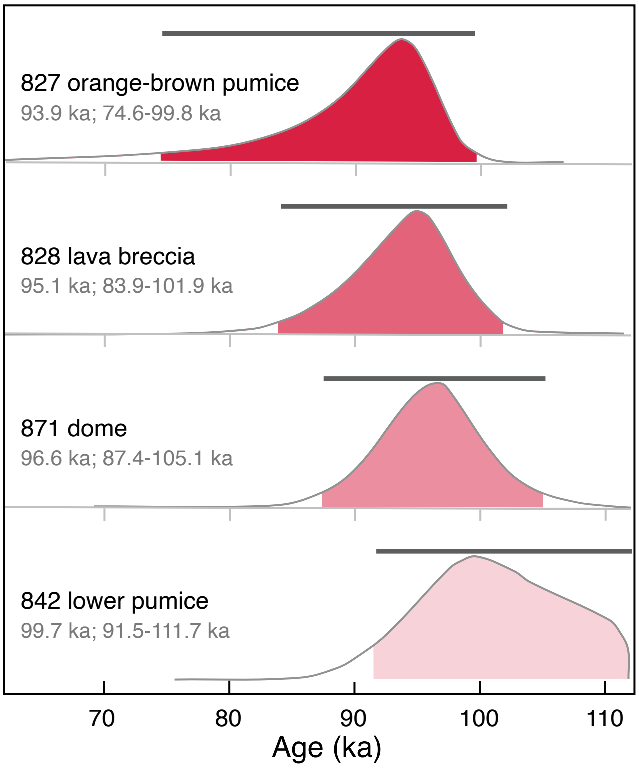
827 orange-brown pumice
93.9 ka; 74.6-99.8 ka
828 lava breccia
95.1 ka; 83.9-101.9 ka
871 dome
96.6 ka; 87.4-105.1 ka
842 lower pumice
99.7 ka; 91.5-111.7 ka
70
80
90
100
110
Age (ka)

Fig. 9

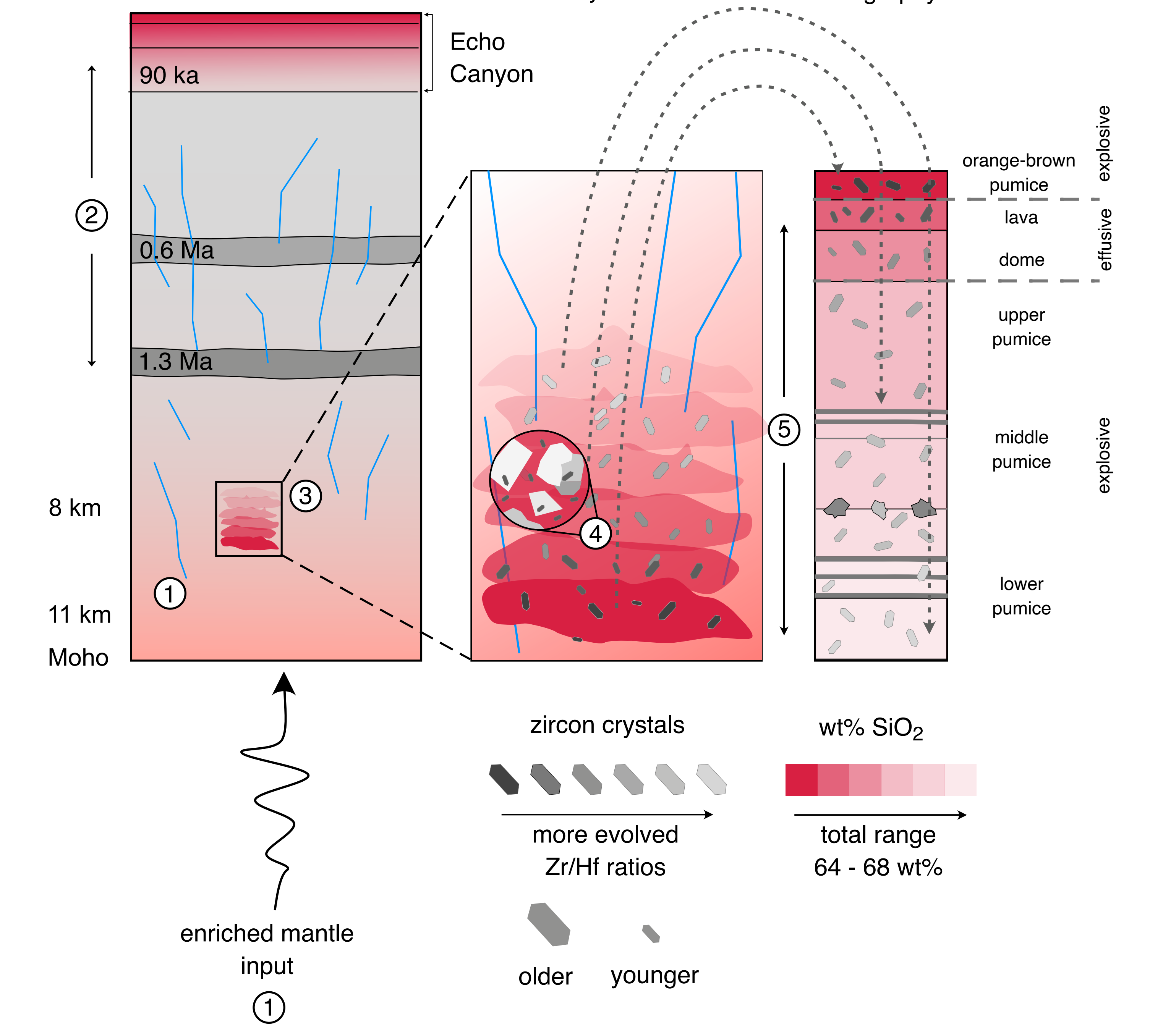
crustal
cross-section
magma
system
trapped EC
stratigraphy
Echo
Canyon
90 ka
0.6 Ma
1.3 Ma
2
3
1
8 km
11 km
Moho
4
5
orange-brown
pumice
lava
dome
upper
pumice
middle
pumice
lower
pumice
explosive
effusive
explosive
enriched mantle
input
1
zircon crystals
more evolved
Zr/Hf ratios
older
younger
wt% SiO2
total range
64 - 68 wt%

Table 1. Stratigraphic, age and analytical information for the Echo Canyon deposits.

	stratigraphic position	sample	ZDD eruption age	U-Th crystallisation isochron age	U-Th-Pb crystallisation age	O isotope range ‰	zircon trace elements	petrographic thin section	XRF major elements	ICPMS trace elements
orange-brown pumice	post-cone	827	93.9 +5.9/-19.3 ka	98.5 +5.9/-5.6 ka MSWD=0.85, n=39	-	-	-	□	□	□
lava breccia	post-cone	828	95.1 +6.8/-11.2 ka	108 +2/-2 ka MSWD=0.94, n=34	-	-	-	□	□	□
dome	post-cone	871	96.6 +8.4/-9.2	111 +4/-4 ka MSWD=0.68, n=55	-	3.40–5.63	□	□	□	□
lower pumice	cone	829	-	-	-	-	-	□	□	□
lower pumice	cone	844	-	113 +15/-14 ka MSWD=0.77, n=16	-	-	-	□	□	□
lower pumice	cone	843	-	-	-	-	-	□	□	□
lower pumice	cone	842	99.7 +1.3/-8.2 ka	108 +10/-9 ka MSWD=0.79, n=17	-	2.67–5.20	□	□	□	□
lithic clast	pre-cone	844F1	-	-	-	-	-	□	□	□
lithic clast	pre-cone	844F2	-	-	0.610 ±0.08 Ma MSWD=0.83, n=3	-	-	□	□	□
lithic clast	pre-cone	844F3	-	-	1.34 ±0.13 Ma MSWD=0.80, n=11	-	-	□	□	□